















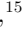



The Mega-MUSCLES Treasury Survey: X-ray to infrared Spectral Energy Distributions of a representative sample of M dwarfs

DAVID J. WILSON ¹, CYNTHIA S. FRONING ², GIRISH M. DUVVURI ³, ALLISON YOUNGBLOOD ⁴, KEVIN FRANCE ^{5,1},
ALEXANDER BROWN ⁶, P. CHRISTIAN SCHNEIDER ⁷, ZACHORY BERTA-THOMPSON ⁵, ANDREA P. BUCCINO ⁸,
JEFFREY LINSKY ⁹, R. O. PARKE LOYD ¹⁰, YAMILA MIGUEL ^{11,12}, ELISABETH NEWTON ¹³, J. SEBASTIAN PINEDA ⁵,
SETH REDFIELD ¹⁴, AKI ROBERGE ⁴, SARAH RUGHEIMER ¹⁵ AND MARIELA C. VIEYTES ¹⁶

¹Laboratory for Atmospheric and Space Physics, University of Colorado, 600 UCB, Boulder, CO 80309

²Southwest Research Institute, 6220 Culebra Road, San Antonio, TX 78238, USA

³Department of Physics and Astronomy, Vanderbilt University, Nashville, TN 37235, USA

⁴NASA Goddard Space Flight Center, Greenbelt, MD 20771

⁵Department of Astrophysical and Planetary Sciences, University of Colorado, Boulder, CO 80309, USA

⁶Center for Astrophysics and Space Astronomy, University of Colorado, 389 UCB, Boulder, CO 80309

⁷Hamburger Sternwarte, Gojenbergsweg 112, 21029 Hamburg

⁸Dpto. de Física, Facultad de Ciencias Exactas y Naturales (FCEN), Universidad de Buenos Aires (UBA), Buenos Aires, Argentina

⁹JILA, University of Colorado and NIST, Boulder, CO 80309-0440 USA

¹⁰Eureka Scientific, Inc., Oakland, CA 94602, USA

¹¹Leiden Observatory, P.O. Box 9500, 2300 RA Leiden, The Netherlands

¹²SRON Netherlands Institute for Space Research, Niels Bohrweg 4, 2333 CA Leiden, The Netherlands

¹³Department of Physics, Massachusetts Institute of Technology, Cambridge, MA 02139, USA

¹⁴Wesleyan University, Department of Astronomy and Van Vleck Observatory, 96 Foss Hill Dr., Middletown, CT 06459, USA

¹⁵Department of Physics and Astronomy, York University, 4700 Keele Street, Toronto, ON M3J 1P3, Canada

¹⁶Instituto de Astronomía y Física del Espacio (CONICET-UBA), Buenos Aires, Argentina

(Received October 8, 2024; Revised November 1, 2024; Accepted November 5, 2024)

Submitted to ApJ

ABSTRACT

We present $5\text{--}1\times 10^7$ Å spectral energy distributions (SEDs) for twelve M dwarf stars covering spectral types M0–M8. Our SEDs are provided for community use as a sequel to the Measurements of the Ultraviolet Spectral Characteristics of Low-mass Exoplanetary Systems (MUSCLES) survey. The twelve stars include eight known exoplanet hosts and four stars chosen to fill out key parameter space in spectral type and rotation period. The SEDs are constructed from Hubble Space Telescope ultraviolet spectroscopy and XMM Newton, Chandra and/or Swift X-ray observations and completed with various model data, including Lyman α reconstructions, PHOENIX optical models, APEC coronal models and Differential Emission Measure models in the currently-unobservable Extreme Ultraviolet. We provide a complete overview of the Mega-MUSCLES program, including a description of the observations, models, and SED construction. The SEDs are available as MAST High-Level Science Products and we describe the various data products here. We also present ensemble measurements from our sample that are of particular relevance to exoplanet science, including the high-energy fluxes in the habitable zone and the FUV/NUV ratio. Combined with MUSCLES, Mega-MUSCLES provides SEDs covering a wide range of M dwarf spectral types and ages such that suitable proxies for any M dwarf planet host of interest may be found in our sample. However, we find that ultraviolet and X-ray fluxes can vary even between stars with similar parameters, such that observations of each exoplanet host star will remain the gold standard for interpreting exoplanet atmosphere observations.

Keywords: M dwarf stars, Exoplanets, Ultraviolet astronomy, X-ray astronomy,

1. INTRODUCTION

M dwarf stars, with masses $\approx 0.1 - 0.5 M_{\odot}$, have emerged as the premier targets for exoplanet discovery and characterization over the past two decades (Tarter et al. 2007), particularly for rocky planets with masses and radii comparable to that of Earth in orbits within the habitable zone around the host star. The focus on M dwarfs is partly due to their great abundance, representing over 70% of stars (Henry et al. 2006), but mostly for observational considerations. The sensitivity of both of the dominant techniques for exoplanet discovery, the transit and radial velocity methods, scale dramatically and favourably with decreased stellar mass, such that planets with similar mass and radius to the Earth are much easier to find around M dwarfs than around larger stars. Additionally, the habitable zones of M dwarfs are much closer in compared to the habitable zones around larger stars due to their lower luminosity, so the orbital periods of planets there are of order days to weeks rather than years, requiring less time-on-target to detect and confirm. Short orbital periods, and a relatively small planet-to-star size ratio, also makes M dwarf planets favourable targets for atmospheric characterisation via transit spectroscopy. The importance of M dwarfs to exoplanet science has been highlighted by some of the most remarkable discoveries, such as the habitable zone planet orbiting Proxima Centauri (Anglada-Escudé et al. 2016) and the seven Earth-sized planets around TRAPPIST-1 (Gillon et al. 2016, 2017). The launch of JWST has enabled an increasing number of atmospheric observations of planets orbiting M dwarfs, ruling out thick atmospheres around several of the most accessible targets (Greene et al. 2023; Zieba et al. 2023; Lincowski et al. 2023; Moran et al. 2023). With the advent of the Rocky Worlds program (Redfield et al. 2024), continued JWST observations of planets around M dwarfs are guaranteed for years to come.

When attempting to assess the characteristics and potential habitability of such planets, we must be cautious when comparing them with the Solar system (Rugheimer et al. 2015a; Rugheimer & Kaltenecker 2018). The differences between M dwarfs and Sun-like stars are many. Their lower temperature means that the spectrum is shifted into the red, and the average M dwarf is much more active than more massive stars, both in terms of flare frequency and maximum flare strength relative to its luminosity (Loyd et al. 2018b; Froning et al. 2019), with the potential effects on their planets exacerbated by the close-in habitable zones (Buccino et al. 2007; Vida et al. 2017).

Perhaps the starkest difference between M dwarfs and Sun-like stars are their high energy spectral energy distributions (SEDs). Multiple observations have demonstrated that the X-ray fluxes of M dwarfs relative to their bolometric luminosities can be thousands of times higher than for Sun-like stars (Wheatley et al. 2017; Wright et al. 2018; Brown et al. 2023). Conversely, the red-ward shift of the photospheric spectrum results in relative near-ultraviolet flux ratios being lower than Sun-like stars by a similar factor. The X-ray and ultraviolet fluxes are key drivers of exoplanet atmospheric structure and chemistry. Photochemistry in the upper atmospheres of exoplanets (i.e., the layers that we can most readily observe) is governed by the incident ultraviolet spectrum, and in particular the strength of the Lyman α line and the ratio of FUV to NUV fluxes (Segura et al. 2005; Moses et al. 2013; Miguel et al. 2015; JWST Transiting Exoplanet Community Early Release Science Team et al. 2023). X-ray and EUV radiation drives atmospheric escape, such that planets in extreme XUV environments may not retain atmospheres at all (Watson et al. 1981; Poppenhaeger et al. 2024; Van Looveren et al. 2024).

A number of surveys have been pursued over the last several years to use HST and other facilities to obtain energetic spectra of M dwarf stars. Programs like Living with a Red Dwarf, HAZMAT, MUSCLES, and FUMES, plus observations focused on individual targets of interest, have greatly expanded the sample of M stars with observed ultraviolet spectra (Guinan et al. 2016; Loyd et al. 2021, 2018a; France et al. 2016; Youngblood et al. 2016; Loyd et al. 2016, 2018b; Bourrier et al. 2017; MacGregor et al. 2021; Waalkes et al. 2019; Diamond-Lowe et al. 2022; Pineda et al. 2021a; Feinstein et al. 2022; Rockcliffe et al. 2021).

Ideally, a full X-ray through optical SED should be obtained for any M dwarf of interest, but such observations are often impractical for multiple reasons. Whilst the high energy emission from M dwarfs is a higher fraction of the bolometric flux relative to a larger star, it is still intrinsically faint, requiring large investments of limited space telescope observing time for even the closest M dwarfs. Accordingly, the MUSCLES Treasury Survey was conceived to provide complete SEDs for a representative sample of low mass stars, while also providing scaling relations for other surveys with more targets but less wavelength coverage (Youngblood et al. 2017).

MUSCLES used HST in combination with X-ray facilities and optical photospheric model atmospheres to obtain 5 Å – 5.5 μm spectral energy distributions (SEDs) for seven M dwarf and four K dwarf stars. High-level data products were

delivered to MAST as a resource for the exoplanet modeling community as well as stellar astrophysicists to provide a uniform ultraviolet survey for the study of M dwarfs that includes reliable measurements of Ly α and resolved stellar emission lines. The MUSCLES SEDs High Level Science Product archive¹ has been used in a number of theoretical studies to model the atmospheric properties of exoplanet atmospheres (Spake et al. 2018; Wunderlich et al. 2020; Kawashima et al. 2019), predict observable atmospheric signatures that can be detected with the JWST (Morley et al. 2017), and investigate the effects of stellar flares on planetary atmospheres and potential life (Miguel et al. 2015; Louca et al. 2023).

The original MUSCLES survey focused on stars with known exoplanets. Given the known nearby systems at the time, largely found by optical radial velocity searches, this resulted in a sample that was biased toward the higher mass end of the M dwarf sequence. Only three MUSCLES targets, GJ 1214, GJ 1061 and Proxima Centauri, had masses below $<0.3 M_{\odot}$. With the launch of JWST, the search for “Earth-like” planets is moving toward the low mass end of the stellar Main Sequence. Surveys including MEarth, TRAPPIST/SPECULOOS, and TESS are finding Earth-sized planets around stars with masses of $\sim 0.3 M_{\odot}$ or below (Berta-Thompson et al. 2015; Dittmann et al. 2017; Winters et al. 2019; Pidhorodetska et al. 2021). It is targets like these, around low mass stars, that will be the subject of atmospheric characterization of rocky planets in the next decade or more (Kempton et al. 2018; Fortenbach & Dressing 2020; Redfield et al. 2024).

It was with this in mind that the Mega-MUSCLES Treasury Survey was conceived as the successor to MUSCLES. Mega-MUSCLES observed thirteen M dwarfs across a range of mass, age, and activity levels (Figure 1), with a particular focus on low mass M stars that are the likely first targets for atmospheric characterization of Earth-like planets. The sample list included observations for six more of the closest low-mass exoplanet host stars; for slow-rotating stars to $0.14 M_{\odot}$ (to serve as proxies for future habitable planet hosts); for stars like GJ 1132 but with faster rotation periods (to track XUV evolution with age); for the 2nd (GJ 699 = Barnard’s Star) and 7th (GJ 729) closest star systems; and for the multiple rocky planet system, TRAPPIST-1. The target list included stars with no known exoplanets that filled out the phase space of M dwarf mass and rotation/activity. When combined with the existing observations, the complete Mega-MUSCLES library spans a range of stellar masses ($0.14\text{--}0.8 M_{\odot}$), high to low X-ray luminosity fraction (an indicator of activity level), and planetary systems ranging from Jupiters to super-Neptunes to super-Earths.

In this paper, we present an overview of the Mega-MUSCLES Treasury Survey. Several papers have already been published focusing on individual targets of interest (Froning et al. 2019; France et al. 2020; Wilson et al. 2021), describing the X-ray observations for both MUSCLES and Mega-MUSCLES in detail (Brown et al. 2023), using the observations to probe proxies of stellar coronal and chromospheric behavior (Linsky et al. 2020), and developing optical proxies for high energy emission (Melbourne et al. 2020). This paper will focus on summarizing the survey observing methods, SED generation, and analysis of the data as a population.

2. OBSERVATIONS AND DATA REDUCTION

2.1. Survey Design

The plan for the original MUSCLES survey was to obtain complete spectral coverage of the 1150–3100 Å waveband at moderate spectral resolution of a representative sample of optically inactive M stars with known exoplanet companions. To this end, the team employed the Cosmic Origins Spectrograph (COS, Green et al. 2012) and the Space Telescope Imaging Spectrograph (STIS, Woodgate et al. 1998) onboard HST to obtain ultraviolet and optical spectroscopy using the COS G130M, G160M, and G230L gratings to cover the FUV and faint NUV (1750–2200 Å) continuum emission and STIS G140M and G230L to observe Lyman α and broadband NUV (France et al. 2016). They also included STIS G430L mode to obtain observationally inexpensive optical spectra at the same epoch as the ultraviolet observations. Finally, the survey included contemporaneous X-ray observations to provide high energy coverage and additional constraints on estimates of the unobservable EUV emission.

For Mega-MUSCLES, we started with the same observing strategy. However, there were some changes made in response to new observatory policies and restrictions. First, we removed the request for coordinated ultraviolet and X-ray observations given the increasing challenges of scheduling multiple observatories together, particularly HST and Chandra. Second, we relaxed the requirement that all the HST visits be executed within one day of each other to ease scheduling pressure. Since the timescale for M dwarf flares is much shorter than the previous one day gap between the

¹ <https://archive.stsci.edu/prepds/muscles/>

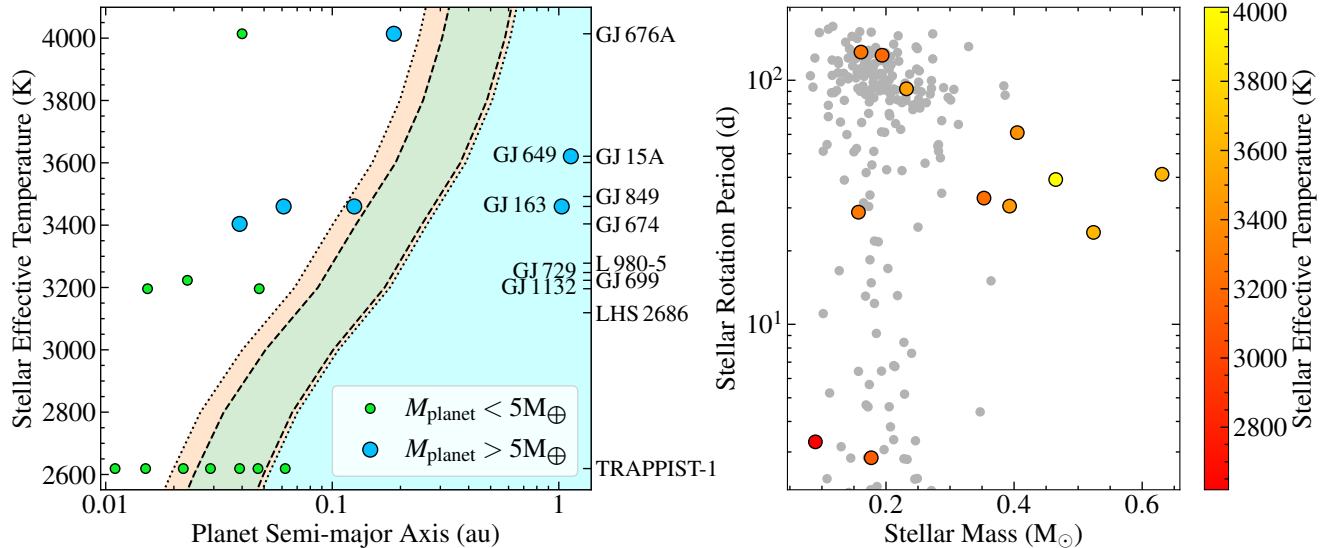


Figure 1. Left panel: Conservative (green) and optimistic (orange) Habitable Zones from Kopparapu et al. (2014) as a function of stellar effective temperature for the Mega-MUSCLES sample, along with their planetary systems (Table 1). Note that GJ 849 b & c are off the x-axis scale at 2.409 au and 4.974 au respectively. Right panel: Stellar masses, temperatures and rotation periods for the Mega-MUSCLES sample. Stars from Newton et al. (2018) are shown in grey for comparison.

COS and STIS visits, there was no motivation to maintain this requirement. Finally, due to the heightened interest within the community for ultraviolet observations of M dwarfs, HST introduced more stringent policies for clearing M dwarfs under bright object protection (BOP) restrictions. This caused us to migrate the observing modes for several targets from COS G130M/G160M to STIS G140L and, for a few stars, STIS G140L to E140M. For all our targets, we preserved the 5 orbit FUV monitoring observations to establish a baseline on time variability and search for flares. Tables 1 and 2 list the targets observed and their stellar and exoplanet properties, while Table 4 summarizes the ultraviolet and X-ray observations of each target ².

2.2. Wavelength region definitions

Throughout the paper we refer to distinct wavelength regions of the SED, the literature definitions of which can vary. Unless specified otherwise, we follow the definitions used for the MUSCLES program by France et al. (2016): X-ray: 5–100 Å; Extreme Ultraviolet (EUV): 100–911 Å; Far Ultraviolet (FUV): 911–1700 Å; Near Ultraviolet (NUV): 1700–3200 Å and optical/IR: >3200 Å.

2.3. Ultraviolet and Optical

We obtained ultraviolet (1150–3200 Å) spectroscopy using COS and STIS under HST Program ID 15071. In most cases observations were obtained in photon-counting time-tagged mode to allow for time-resolved light curves and spectra. The spectral resolving power varied depending on observing mode: $R = 45,800$ for STIS E140M, $R \sim 10,000$ for STIS G140M, $R \sim 15,000$ for COS G130M/G160M, $R \sim 3,000$ for COS G230L, $R \sim 2,000$ for COS G140L, $R \sim 1,000$ for STIS G140L, and $R \sim 500$ for STIS G230L.

For each target, we obtained longer (5 orbit) observations in the FUV using either COS G130M (1150–1450 Å), COS G140L (1150–1700 Å), or STIS G140L (1150–1700 Å). The default grating setting for COS G130M was the 1291 Å mode; however, for five targets (GJ676A, GJ649, GJ674, GJ699, and LHS2686), we switched to G130M/1222 to move the BOP-violating Si IV 1393,1402 Å doublet off the detector; the long cutoff for those monitoring observations is 1365 Å. For the two stars that were too bright for both COS and the STIS first-order gratings (GJ 15A and GJ 729), we used the STIS E140M echelle grating. This had the added benefit of covering the Lyman α line at high resolution.

² The M4.5 star LP 756-18 was also observed as part of the Mega-MUSCLES program. Unfortunately the observations failed due to guide star acquisition failures, with only a single STIS G430L exposure returning a usable spectrum (dataset ODLM30010). We therefore do not include LP 756-18 in the Mega-MUSCLES sample or HLSF, but note it here to avoid confusion with, for instance, earlier publications that may mention it as part of the survey.

Table 1. Mega-MUSCLES Target Summary

Star	Distance (pc)	Spectral Type	P_{Rot} days	Exoplanet Mass (M_{\oplus})	Semi-major Axis (au)	Active? ^a	Refs
GJ676A	16.0	M0 V	41.2	4.4 ^b , 11.5 ^b , 2127, 2161 ^b	0.04, 0.187, 1.8152, 6.6	N	1
GJ15A	3.6	M2 V	30.5	5.35 ^b	0.072	N	2,3, 18
GJ649	10.4	M1 V	23.8	87.4 ^b	1.13	N	4,5,19,20
GJ674	4.6	M3 V	32.9	11.1 ^b	0.039	N	6,7,21
GJ729	3.0	M3.5 V	2.8	Y	2,3,8
GJ163	15.1	M3.5 V	61	10.6 ^b , 6.8 ^b , 29.0 ^b	0.061, 0.125, 1.03	N	1,9
GJ1132	12.6	M4 V	126.6	1.66, 2.64 ^b	0.0153, 0.0476	N	10,11,22
L980-5	13.3	M4 V	92.2	N	11
GJ849	8.8	M3.5 V	39.2	283 ^b , 342.9 ^b	2.409, 4.974	N	1,5,20,23,24
GJ699	1.8	M4 V	130.4	0.37 ^b	0.02294	N	12,13, 27
LHS2686	12.2	M5 V	28.8	Y	
TRAPPIST-1	12.1	M7.5 V	3.3	1.017, 1.156, 0.297 0.772, 0.934 1.148, 0.331	0.011, 0.015, 0.022 0.029, 0.039 0.047, 0.062	Y	14,15,25,26

NOTE—Distances taken from Gaia DR2 (Gaia Collaboration et al. 2018, 2016). Rotational period references: 1 (Suárez Mascareño et al. 2015), 2 (Newton et al. 2016), 3 (Allen & Herrera 1998), 4 (Díez Alonso et al. 2019), 5 (Veyette & Muirhead 2018), 6 (Kiraga & Stepien 2007), 7 (Montes et al. 2001), 8 (Ibañez Bustos et al. 2020), 9 (Bonfils et al. 2013), 10 (Newton et al. 2018), 11 (Berta-Thompson et al. 2015), 12 (Toledo-Padrón et al. 2019), 13 (Ribas et al. 2018), 14 (Vida et al. 2017), 15 (Burgasser & Mamajek 2017). Exoplanet properties references: 16 (Anglada-Escudé & Tuomi 2012), 17 (Sahlmann et al. 2016), 18 (Howard et al. 2014), 19 (Johnson et al. 2010), 20 (Rosenthal et al. 2021), 21 (Bonfils et al. 2007), 22 (Bonfils et al. 2018), 23 (Butler et al. 2006), 24 (Montet et al. 2014), 25 (Gillon et al. 2016), 26 (Grimm et al. 2018), 27 (Gonzalez Hernandez et al. 2024).

^aOptical activity designation where “Y” (Yes) indicates targets for which H α is in emission (Newton et al. 2017)

^b $M \sin i$

Table 2. Stellar parameters for the Mega-MUSCLES sample reproduced from Table 3 of Pineda et al. (2021b).

Name	L_{bol} (10^{31} erg s ⁻¹)	Mass (M_{\odot})	Radius (R_{\odot})	T_{eff} (K)
TRAPPIST-1	0.234 \pm ^{0.009} _{0.008}	0.090 \pm ^{0.003} _{0.002}	0.120 \pm 0.006	2619 \pm ⁷¹ ₆₆
LHS 2686	1.078 \pm 0.024	0.157 \pm 0.004	0.182 \pm 0.008	3119 \pm ⁷⁰ ₆₈
GJ 699	1.302 \pm ^{0.024} _{0.023}	0.1610 \pm ^{0.0036} _{0.0035}	0.187 \pm 0.001	3223 \pm 17
GJ 729	1.537 \pm 0.018	0.177 \pm 0.004	0.200 \pm 0.008	3248 \pm ⁶⁸ ₆₆
GJ 1132	1.668 \pm ^{0.049} _{0.047}	0.194 \pm 0.005	0.215 \pm 0.009	3196 \pm ⁷¹ ₇₀
L 980-5	2.488 \pm ^{0.079} _{0.078}	0.232 \pm 0.006	0.250 \pm 0.010	3278 \pm ⁷⁴ ₇₀
GJ 674	6.03 \pm 0.14	0.353 \pm 0.008	0.361 \pm ^{0.012} _{0.011}	3404 \pm ⁵⁹ ₅₇
GJ 15A	8.608 \pm 0.069	0.393 \pm ^{0.009} _{0.008}	0.385 \pm 0.002	3601 \pm ¹² ₁₁
GJ 163	8.28 \pm 0.24	0.405 \pm 0.010	0.409 \pm ^{0.017} _{0.016}	3460 \pm ⁷⁶ ₇₄
GJ 849	11.051 \pm ^{0.095} _{0.094}	0.465 \pm 0.011	0.464 \pm 0.018	3492 \pm ⁷⁰ ₆₈
GJ 649	16.74 \pm 0.170	0.524 \pm 0.012	0.531 \pm 0.012	3621 \pm ⁴¹ ₄₀
GJ 676A	34.04 \pm ^{0.84} _{0.80}	0.631 \pm 0.017	0.617 \pm ^{0.028} _{0.027}	4014 \pm ⁹⁴ ₉₀

The NUV spectra of those stars were obtained with the STIS/CCD G230LB grating instead of G230L. For stars without E140M observations we used STIS G140M to observe Lyman α at moderate spectral resolution. In addition to the ultraviolet observations, one of the STIS visits for each star included two consecutive short exposures (with the time varying by star) using the CCD G430L setting, covering 2900–5700 Å at a resolving power of $R \sim 500$.

We extracted light curves from all time-tagged observations to search for stellar flares. For STIS, we used the STISTOOLS³ inttag routine to split the tag files into 20s chunks, then extracted a spectrum from each chunk and integrated it to produce a light curve. For COS, light curves were extracted from the corrtag event files for each exposure by summing the counts around the location of the spectral trace in the 2-D event list and subtracting background regions of the same size offset in the cross-dispersion direction.

The spectra were downloaded from the MAST archive after they had been processed using the default CALCOS and CALSTIS data reduction pipelines. For COS observations covering more than one orbit, we shifted each spectrum to the same wavelength scale based on cross-correlation of strong emission lines before coadding, providing a small S/N ratio advantage over the standard x1dsum spectra. In four cases (GJ 1132, GJ 163, LHS-2686 and TRAPPIST-1) the automated CALSTIS pipeline failed to identify the correct spectral trace in some or all of the G140M observations. We re-extracted these spectra using the STISTOOLS routines, visually identifying the a2center parameter (the y-position of the spectral trace on the detector from the fit files. Once vetted and, if necessary, re-extracted, STIS spectra for each grating were combined using a variance-weighted average.

All of the HST data from program 15071 can be found in MAST: [10.17909/jq0n-jh43](https://mast.stsci.org/#/search/10.17909/jq0n-jh43).

2.4. X-ray

A full description of the x-ray observations used by MUSCLES and Mega-MUSCLES is presented in [Brown et al. \(2023\)](#), so we briefly summarise here. Six stars were observed with the ACIS-S3 instrument onboard the Chandra X-ray Observatory (Chandra), five as part of the Mega-MUSCLES program (GJ 15A, GJ 163, GJ 849, GJ 699, LHS 2686, program id 19200772 PI Froning), and one retrieved from archival data (L980-5, program 81200661, PI Wright). A further five stars were observed with XMM-Newton (XMM) using the EPIC detectors, with four dedicated observations (GJ 649, GJ 674, GJ 729, TRAPPIST-1, program 081021, PI Froning) and another archival dataset (GJ 1132, program 080493, PI King). Finally, we retrieved archival observations of GJ 676A obtained with the XRT on the Neil Gehrels Swift Observatory (Swift). X-ray exposure times for each target are given in Table 4.

3. SED CONSTRUCTION

The construction of the SEDs builds on the techniques used for the MUSCLES sample by [Loyd et al. \(2016\)](#), but with multiple changes and improvements. Most notably, we now include estimated uncertainties for the portions of the SEDs filled with models. The final SEDs for all twelve stars are shown in Figures 2 and 3.

3.1. X-ray

X-ray data were fit using the XSPEC package (Versions 12.5.1-12.12.0 [Arnaud 1996](#)). Each spectrum was fit with a combination of an Astrophysical Plasma Emission Code (APEC, [Smith et al. 2001](#); [Foster et al. 2012](#)) model with 1–3 temperatures depending on the quality of the spectrum, modified by absorption from a fixed interstellar hydrogen column density, typically $N_{\text{H}} = 10^{18-19} \text{ cm}^{-2}$ (small enough that the effects on the analysis are minimal). The models were then used to fill in the gaps between the end of the X-ray spectra (varied by star) and the lowest wavelengths of the EUV models ($\approx 120\text{Å}$). The XMM spectra were adjusted for photon losses at the low energy boundary as described in [Wilson et al. \(2021\)](#). In two cases spectra were unavailable: GJ 676A where only a low count rate from Swift was recovered, and L 980-5, which was not detected by Chandra. We therefore use APEC models for the entire X-ray region for those stars, fit to the Swift flux measurement and the Chandra upper limits respectively. See [Brown et al. \(2023\)](#) for more details.

Uncertainties for the APEC models were generated via a Monte-Carlo approach. For each star, we generated 10,000 models with each parameter randomly drawn from a normal distribution defined by their best fit and 1σ statistical uncertainty values. This produced a normal distribution for each wavelength bin, from which we take the mean and standard deviation as the final flux and error values respectively.

³ <https://stistools.readthedocs.io/en/latest/index.html>

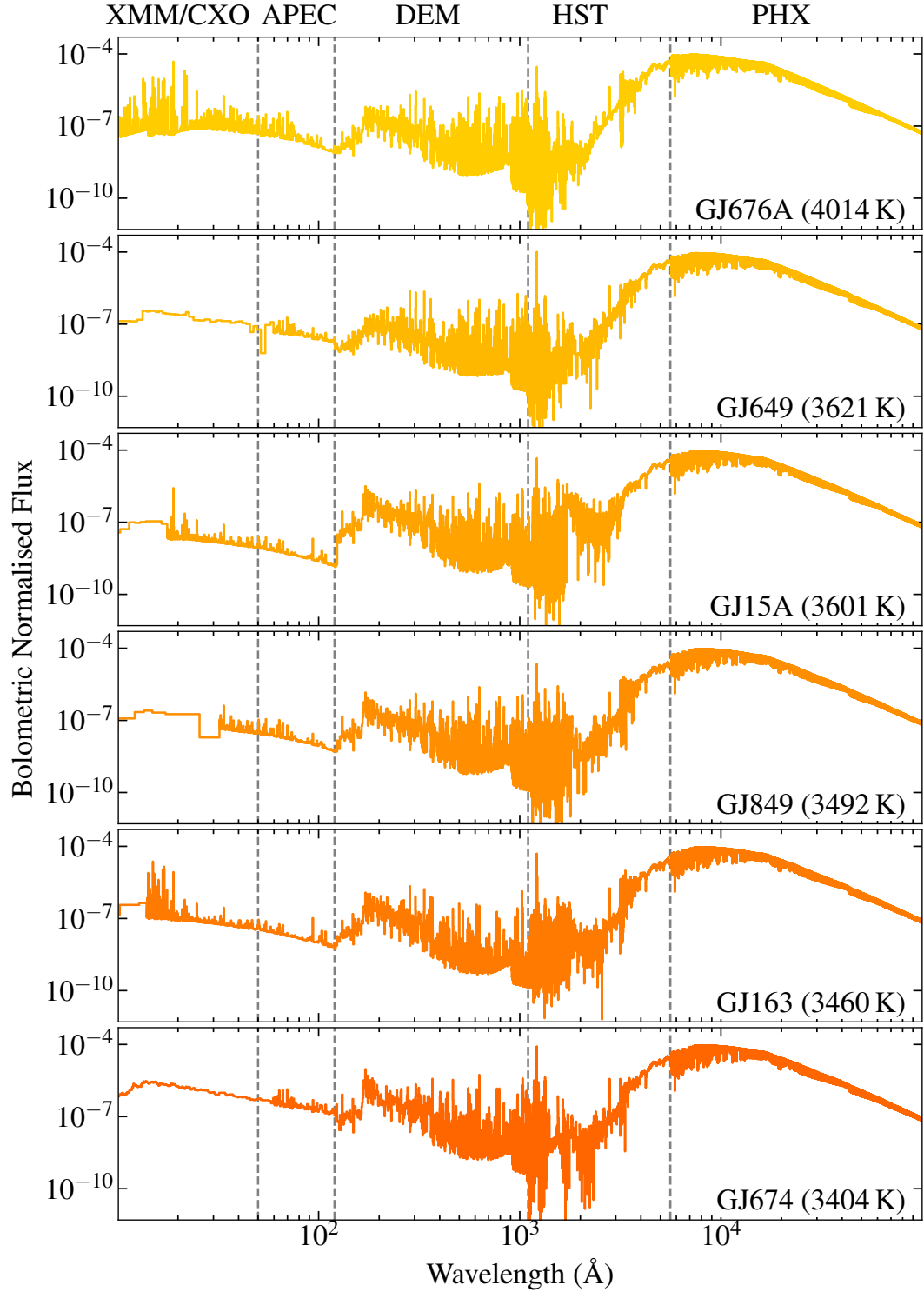


Figure 2. The first six Mega-MUSCLES SEDs in descending order of T_{eff} . The lines delineating the various data sources are approximate as the exact breaks vary depending on, for example, the S/N of the observed spectra.

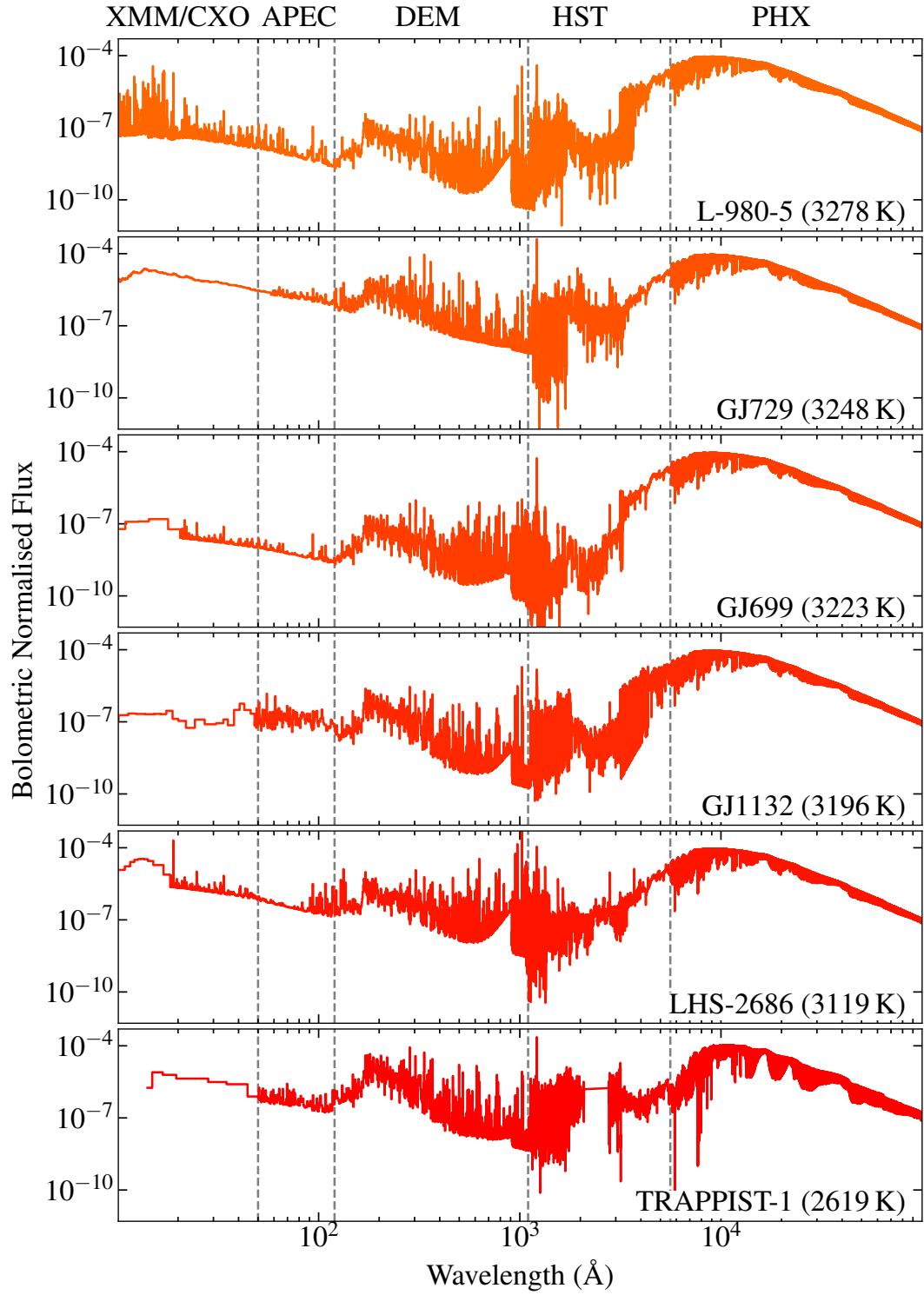


Figure 3. The remainder of the SEDs in descending order of T_{eff} .

3.2. Extreme Ultraviolet

The EUV region is currently unobservable for the most part, due to a combination of interstellar hydrogen absorption in the range 400–900 Å and a lack of sufficiently sensitive instruments at other wavelengths. Mega-MUSCLES SEDs therefore use two different model treatments for the EUV flux.

The initial release of the Mega-MUSCLES SEDs in early 2022 used the [Linsky et al. \(2014\)](#) empirical scaling relations for the EUV region, whereby the integrated flux of the Lyman α line ($F_{\text{Ly}\alpha}$, Section 3.3.1) is converted into an EUV flux in 9 wavelength bands, up-sampled to 1 Å bins. This is the same treatment used in MUSCLES. The only inputs for the EUV scaling relationships are the Lyman α flux and spectral type, so to estimate the uncertainty we generated models with inputs of $F_{\text{Ly}\alpha} + \sigma_{\text{Ly}\alpha}$ and $F_{\text{Ly}\alpha} - \sigma_{\text{Ly}\alpha}$, and used the mean difference of these models from the model generated with $F_{\text{Ly}\alpha}$ as the uncertainty values.

However, these bandpass flux relations are calibrated with a limited sample of stars that are not representative of the broader exoplanet host population. In the updated release accompanying this paper, the EUV regions are instead estimated using Differential Emission Measure models. The “differential emission measure” technique, or DEM, is an empirically informed but physically constrained method to use observed emission features to constrain the density and temperature structure of the plasma being observed. By assuming that the plasma is collisionally dominated and optically thin, the flux of an emission line can be expressed as the integral of the product of two functions, an “emissivity” or “contribution function” that is calculable from atomic data for the line, and an “emission measure” function which describes the total amount of plasma emitting the line. Many formulations of both functions exist (see [Mariska 1992](#) for an overview), and the DEM conceptualizes the emission measure as a function of how many collisions along the line of sight excite the line’s upper state. The majority of the FUV lines listed in Table 5 form over narrow ranges of temperature in the transition region (the Fe XII and Fe XXI are coronal exceptions) while the observed X-ray spectrum is largely formed in the corona, making it possible to fit the DEM across a wide range of temperatures. Each measured flux is a localized-in-temperature constraint on what model DEM best fits the data given the calculated contribution function associated with the flux measurement. With a set of likely model DEMs in hand, we can calculate the contribution functions for the emission being formed co-spatially with the the observed features, but at unobserved wavelengths, and calculate the expected flux given the model DEM and calculated contribution function.

[Duvvuri et al. \(2021\)](#) and [Duvvuri et al. \(2023\)](#) developed an implementation of this technique that propagates both the observational uncertainties and a parameterization of the systematic uncertainty associated with the technique’s ability to reproduce the observations forward to the inferred spectrum. These DEM-generated spectra are used for the updated release accompanying this paper and have the advantage of being tailored more specifically to the star using fluxes formed in both the transition region and corona instead of solely the transition region’s Lyman α or the coronal X-ray flux. The provision of a spectrum at finer resolution than 100 Å also benefits science cases like the ionization of species other than hydrogen and solving for the population of the excited state of the He I 10830 Å triplet used to observe atmospheric escape.

The inputs for the DEM are the X-ray spectra/models described above, and measurements of emission line fluxes in the FUV spectra. Table 5 provides a summary of emission line fluxes used here, with the number and species of lines dependent on the coverage and S/N of each spectrum. The lines were fitted with Gaussian profiles convolved with the appropriate Line Spread Function⁴, with Voigt and/or two-component Gaussian profiles used on rare occasions for strong resonance lines.

3.3. Far- and Near- Ultraviolet

FUV and NUV spectra were spliced together, favouring higher resolution data in regions where spectra from different instrument setups overlapped (i.e. favouring COS or STIS E140M spectra). COS spectra are heavily affected by geocoronal airglow from Lyman α and O I. We conservatively removed O I regions covering 1300–1310 Å and 1353–1356 Å from the COS spectra, replacing them with STIS G140L spectra if available and by a two-degree polynomial fit to the 5 Å on each side of the gap if not. For Lyman α we removed the region 1207–1222 Å and replaced it with STIS G140M and the Lyman α reconstruction detailed below.

⁴ <https://www.stsci.edu/hst/instrumentation/cos/performance/spectral-resolution>

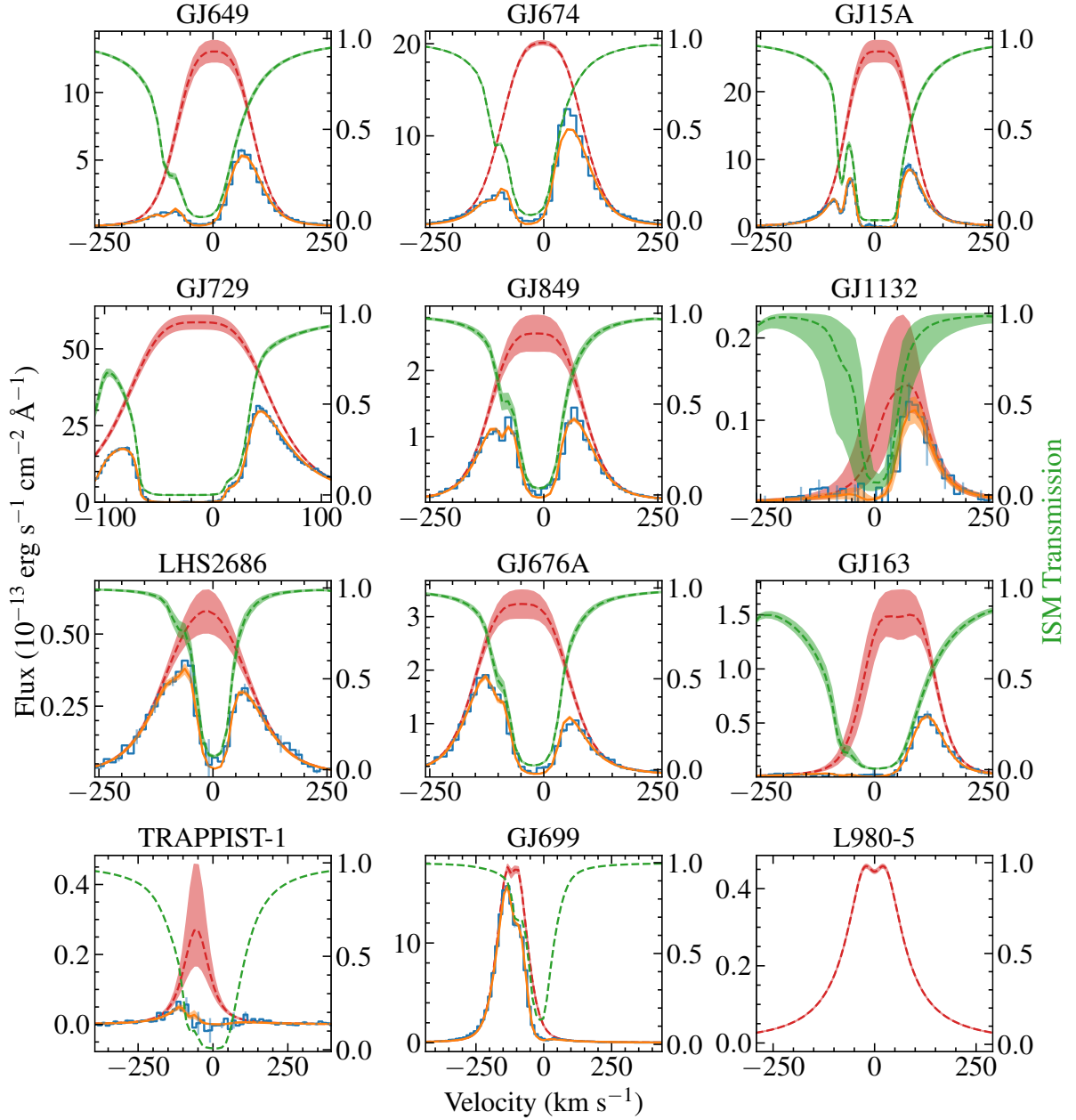


Figure 4. Lyman α profiles for all Mega-MUSCLES stars. Each panel shows the observed G140M or E140M spectrum (blue), the reconstructed intrinsic profile (red), the ISM profile (green, right axis) and the fit to the data, the product of the intrinsic and ISM profiles (orange), all smoothed to their respective instrumental profiles. Shaded regions around each line show the 1σ uncertainty ranges. The profile for L980-5 is a scaled version of the GJ 699 profile (see text) so only the intrinsic profile is shown.

3.3.1. Lyman α

H I 1215.67 \AA Lyman α is by far the brightest emission line in M dwarf ultraviolet spectra (France et al. 2013), but H I gas in the interstellar medium severely attenuates much of the stellar emission. To reconstruct the intrinsic stellar Lyman α flux, we simultaneously fit a model of the interstellar absorption and a model of the intrinsic stellar emission, convolved with the instrument line spread function, to the STIS G140M or E140M spectra. The specifics

Name	$F_{\text{Ly}\alpha}$ (10^{-14} erg s $^{-1}$ cm $^{-2}$ Å $^{-1}$)	log N(H I) (cm $^{-2}$)	Self reversal parameter p
GJ 1132	$0.9^{+0.56}_{-0.23}$	$17.5^{+0.62}_{-0.88}$	$1.34^{+0.3}_{-0.24}$
GJ 15A	$180^{+8.6}_{-8}$	$18.1^{+0.021}_{-0.022}$	$1.02^{+0.036}_{-0.017}$
GJ 163	$11^{+1.5}_{-1.4}$	$18.5^{+0.047}_{-0.06}$	$1.38^{+0.26}_{-0.25}$
GJ 649	$100^{+4.9}_{-4.6}$	$18.2^{+0.02}_{-0.021}$	$1.05^{+0.074}_{-0.036}$
GJ 674	$170^{+1.4}_{-1.4}$	$18^{+0.0066}_{-0.0067}$	$1^{+0.0026}_{-0.0012}$
GJ 676A	$33^{+1.8}_{-1.7}$	$17.8^{+0.055}_{-0.061}$	$1.07^{+0.11}_{-0.052}$
GJ 699	100^{+2}_{-2}	$17.6^{+0.02}_{-0.02}$...
GJ 729	380^{+11}_{-10}	$17.7^{+0.029}_{-0.033}$	$17.72^{+0.03}_{-0.03}$
GJ 849	$25^{+1.8}_{-1.7}$	$17.8^{+0.063}_{-0.071}$	$1.09^{+0.13}_{-0.066}$
L 980-5	$4.4^{+0.9}_{-0.9}$
LHS-2686	$5.7^{+0.39}_{-0.38}$	$17.3^{+0.096}_{-0.13}$	$0.328^{+0.36}_{-0.23}$
TRAPPIST-1	$1.4^{+0.6}_{-0.36}$	$18.4^{+0.1}_{-0.1}$...

Table 3. Parameters of the Lyman α line reconstructions for the Mega-MUSCLES sample. The values for GJ 699 and TRAPPIST-1 were taken from France et al. (2020) and Wilson et al. (2021) respectively, who used a different formulation for self-reversal which did not provide a p value. L 980-5 uses a scaled GJ 699 profile so does not have a measured N(H I).

of the model and fitting process with `emcee` (Foreman-Mackey et al. 2013) are described in detail in Youngblood et al. (2021). In brief summary, we assume Voigt profiles for both the interstellar absorption, stellar emission and self-reversal (Youngblood et al. 2022), fitting a single ISM cloud. Such an assumption is not ideal given the complexity of the local ISM (Redfield & Linsky 2008), but is appropriate given that multiple clouds are likely unresolvable with STIS G140M. We relate the H I and D I absorbers under standard assumptions that they share the same kinematics, are under thermal equilibrium, and have a fixed abundance ratio (see Youngblood et al. 2016, 2021). Figure 4 shows the reconstructed lines for each star, together with the underlying data and models, and Table 3 shows the key fitted parameters.

The Lyman α reconstructions for GJ 699 and TRAPPIST-1 have already been presented in France et al. (2020) and Wilson et al. (2021) respectively, but we restate the results here for completeness. Additionally, no signal was detected from the target in the G140M observations of L 980-5, so estimates of the strength of the Lyman α line were made from five strong emission lines elsewhere in the spectrum (C II 1335 Å, Si IV 1400 Å, C IV 1550 Å, He II 1640 Å and Mg II 2800 Å) along with the rotation rate, via the scaling relationships from Youngblood et al. (2017). By averaging the six estimates we find an estimated integrated Lyman α flux of $(4.4 \pm 0.9) \times 10^{-14}$ erg s $^{-1}$ cm $^{-2}$. As the surface gravity and spectral type of L 980-5 are similar to those of GJ 699, we used the Lyman α profile for Barnard’s Star in the L 980-5 SED, scaled to have the estimated integrated flux and shifted to the correct radial velocity.

The majority of the Mega-MUSCLES Lyman α reconstructions are based on observations with the STIS G140M grating. Wilson et al. (2022) used this grating to observe the Lyman α line of a binary star at different velocities, allowing the line to be observed at different levels of ISM absorption. Reconstructions to those observations returned Lyman α flux differences of up to factor ~ 2 , which they attributed to the inability to properly resolve the D I line. Further work is needed to properly assess the systematic errors in reconstructions based on G140M, but at present the potential for large imprecision in the Lyman α flux should be taken into account in any study that uses the Mega-MUSCLES SEDs. The reconstructions for GJ 15A and GJ 729 are based on E140M data where the D I line is resolved, so should be unaffected by this systematic error.

3.4. STIS flux normalisation

For the MUSCLES sample, Loyd et al. (2016) scaled the fluxes of STIS spectra based on comparisons with overlapping COS data. They found that the STIS data spectra had systematically lower fluxes than the COS data, attributable to slit losses in STIS. For Mega-MUSCLES, we find that significant flux differences between overlapping regions in COS and STIS spectra (either COS G130M compared with STIS G140L or COS G160M compared with STIS G230L) are a) smaller on average than those found for the MUSCLES sample and b) fluxes are higher in STIS, not COS in most cases. The integrated flux from FUV spectra is dominated by emission lines which could genuinely vary between observations, making them an imperfect flux calibrator. Unlike MUSCLES, Mega-MUSCLES has no stars observed

with both COS and STIS in the NUV, where the continuum flux is a major contributor. We therefore chose not to scale the Mega-MUSCLES STIS spectra.

3.5. *Optical*

The blue-optical region of the SED is constructed from two consecutive exposures using the STIS G430L grating, combined in the standard pipeline with a cosmic-ray removal routine. The nominal wavelength coverage of this set up is 2900–5700 Å, but in practice the combination of low detector throughput and the decreasing flux from the target at short wavelengths results in an effective non-detection of the blue end of this range at every star. The MUSCLES SEDs used a fixed cutoff at 3850 Å (Loyd et al. 2016), but for Mega-MUSCLES we chose to vary the cutoff point for two reasons: In some stars the continuum was clearly detected below this region, and, given the excellent flux calibration (see Section 3.5.2) we wanted to retain as much of the spectrum as possible; in other, fainter stars, only higher wavelength regions were detected. We therefore removed all points where the mean flux/flux error ratio of the 30 surrounding bins was less than one. The cut-offs for the various stars range from 3067–4334 Å. Any gaps between the G230L and G430L spectra were filled with the PHOENIX models described below. The spectra and models are shown in Figure 5.

3.5.1. *PHOENIX models*

Given the inhomogeneity of the available optical to infrared spectroscopy, the SED from 5700 Å onwards are filled with a PHOENIX photospheric model spectrum from the Lyon BT-Settl CIFIST 2011.2015 grid (Allard 2016; Baraffe et al. 2015) retrieved from the SVO theoretical web server service⁵. The grid models are given as flux at the surface of the star as a function of T_{eff} and $\log g$.

Stellar parameters for the Mega-MUSCLES sample were taken from Pineda et al. (2021b) and given in Table 2. Full details of the measurements are given in that paper, but in short, K_s , J , and r or V band photometry were combined with the Gaia parallax (Gaia Collaboration et al. 2018) to simultaneously fit the luminosity, mass, radius and T_{eff} of each star via the mass-luminosity relationship of Mann et al. (2019), an empirical mass-radius relationship defined in the paper, and the color-luminosity relationships from Mann et al. (2015). For each star, we used the grid to interpolate a model spectrum for the appropriate parameters, then normalised the spectrum by the squared ratio of the radius and distance. Note that the CIFIST models extend out to wavelengths of 999.5 μm , in contrast to the 5.5 μm cutoff of the Husser et al. (2013) grid used by MUSCLES.

Given the very large number of data points in the spectrum it was computationally prohibitive to calculate errors in the same way as for the APEC models. By retrieving models using the 1σ range for each parameter, we found that the uncertainty on T_{eff} had by far the largest impact on the integrated flux (≈ 1 percent, compared with 0.01 percent for the other parameters). Furthermore, uncertainties in radius and distance are propagated though into the T_{eff} uncertainty by Pineda et al. (2021b). We therefore use the mean difference between models for the given T_{eff} and models for $T_{\text{eff}} \pm 1\sigma$ as a reasonable estimate of the uncertainty.

3.5.2. *Flux calibration*

The G430L spectra obtained for MUSCLES were found to systematically under predict the flux from their targets in comparison with broadband photometry, likely due to slit losses due to imperfect target centering in the slit. To attempt to prevent this issue, the Mega-MUSCLES G430L spectra were obtained with a wider slit (0.2 arcseconds instead of 0.1), reducing the slit losses. We tested the success of this setup by assembling archival flux calibrated spectra from CASLEO and/or X-shooter (Table 6) and Swift U-band photometry. We find that the G430L fluxes obtained from observations with the wider slit are in good agreement with the archival data where available, as shown for GJ 729 in the top panel of Figure 6. We therefore retain the standard pipeline flux calibration for the G430L spectra with no additional scaling.

Figures 5 and 6 also compare the observed spectra with the PHOENIX models. For all stars, we find that the model matches the depths of strong absorption lines, but overpredicts the broad band continuum by a factor of 2–4. This issue has been noted in several works (see for e.g. Fontenla et al. 2015; Peralta et al. 2023), with a general consensus that it is likely due to an incomplete treatment of broad band opacities in the models at blue wavelengths. No applicable solution is currently available, but it should not impact the usability of our SEDs as most of the affected region is covered by the G430L spectra.

⁵ <http://svo2.cab.inta-csic.es/theory/newov2/index.php?models=bt-settl-cifist>

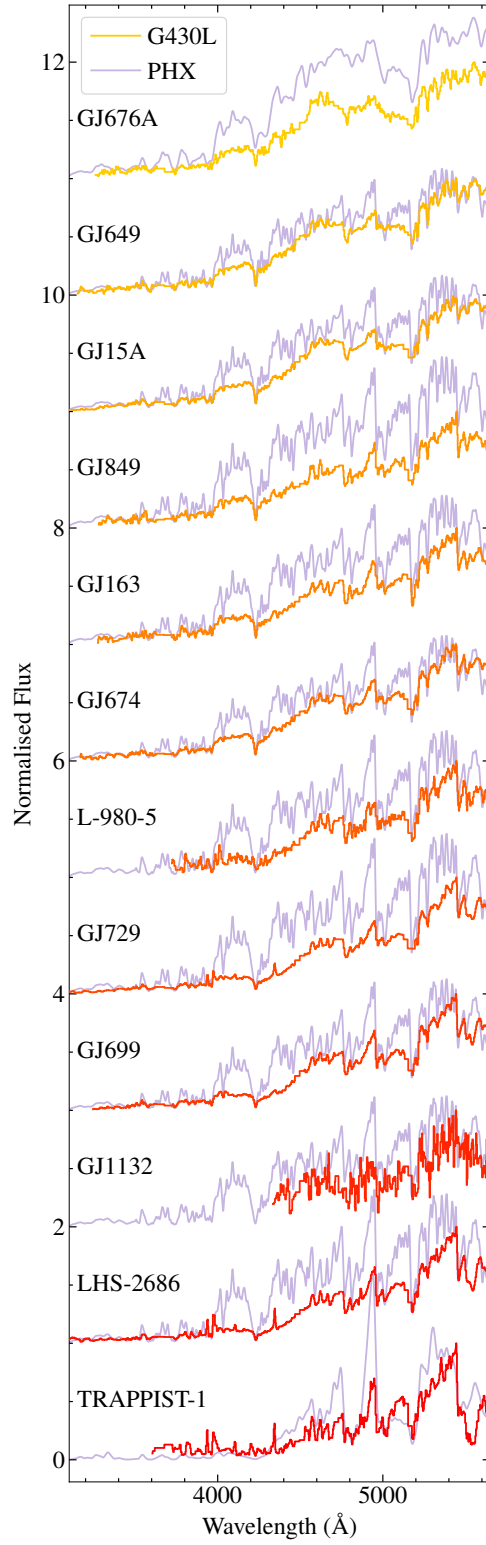


Figure 5. STIS G430L optical spectra for all targets in descending order of T_{eff} , compared with the PHOENIX (PHX) model used for each star. The mismatch between the peaks of the spectra and models is clearly seen at all stars.

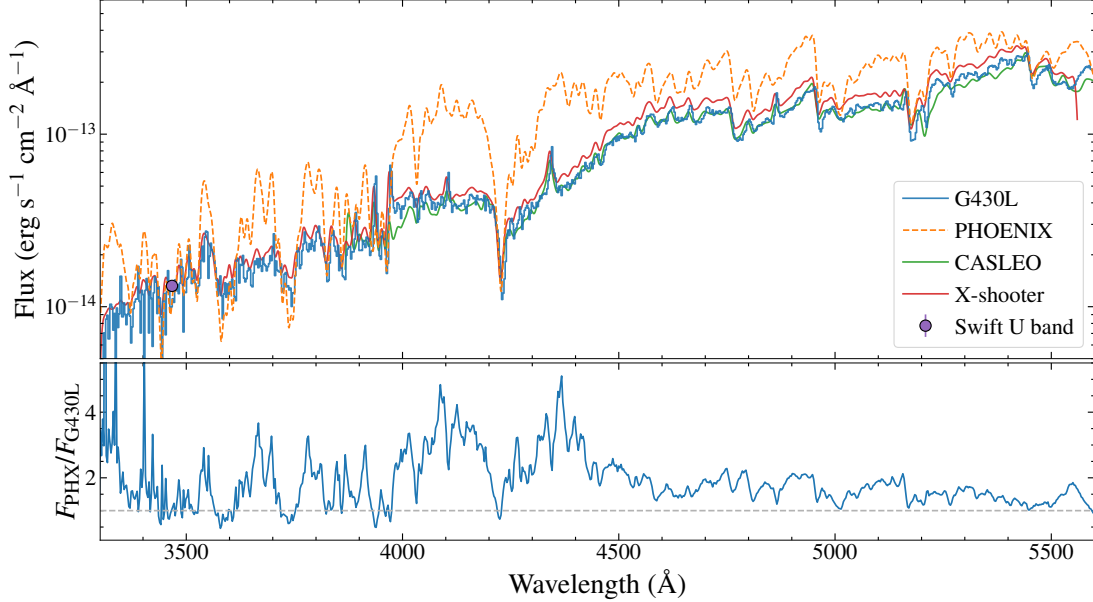


Figure 6. Comparison of blue-optical data of GJ 729, for which the most data is available from our sources. Top panel: Comparison of STIS G430L, CASLEO and X-shooter spectra, as well as Swift U band photometry and the PHOENIX model spectrum. Bottom panel: Ratio between the G430L and PHOENIX spectrum. Similar trends are seen at all other stars.

3.6. Stellar Activity

M dwarfs are notably active stars on multiple timescales (for example, flares on seconds to hours, rotation modulation on days to weeks and stellar activity cycles on months to years), which can strongly affect the X-ray and ultraviolet spectra. Flares can be identified in X-ray and ultraviolet spectroscopy by converting photon-counting/time-tagged data into light curves, and this was done for all suitable observations. We found strong flaring at two stars, each of which is discussed in a separate paper: GJ 674 (Froning et al. 2019) and Barnard’s Star (France et al. 2020). At least one small flare was detected in the time-tag data for all stars except for GJ 1132 and TRAPPIST-1 (the faintest targets). For the large GJ 674 flare the change in integrated flux between spectra with and without the flare included was ≈ 100 percent, but for most flares this difference was much smaller, $\approx 5 - 10$ percent.

With this in mind, combined with the fact that our X-ray and ultraviolet observations were taken at different times, we have chosen *not* to remove the effects of stellar activity from our SEDs. This is the same approach taken by MUSCLES (Loyd et al. 2016). The fluxes of the different regions of the SEDs can therefore be only definitively said to be the fluxes of the star, in that waveband, at the particular time of that observation, and might not necessary represent the time-averaged flux of the star. For the stars without flare detections the fluxes can be reasonably assumed to represent the pseudo-quietest (non-flaring) spectrum of the star, although with the caveat that the X-ray and ultraviolet fluxes might be sampled from different points in the stars rotation and/or activity cycle. Kamgar et al. (2024) found that FUV fluxes for 10 M dwarfs changed by 30–70 percent over time scales of decades, although their data was in most cases too sparse to reliably match it to stellar rotation periods or cycles. (Loyd et al. 2023) used extensive FUV observations of the M 2.5V star GJ 436 to find a ≈ 40 percent change in flux due to activity cycles with an ≈ 8 percent change from rotational modulation. To truly characterise the time-averaged ultraviolet spectra of these stars would require extensive repeat observations, which are unfeasible with our current facilities, but our data and these studies suggest that the contributions from flares, activity cycles and rotation periods are all of order 10s of percent.

3.7. Final Spectral energy distributions and data products

Figure 2 and 3 show the final assembled SEDs for our 12 targets, the combination of the various spectra and models described in the previous subsections. Our final products are publicly available for retrieval from the MUSCLES

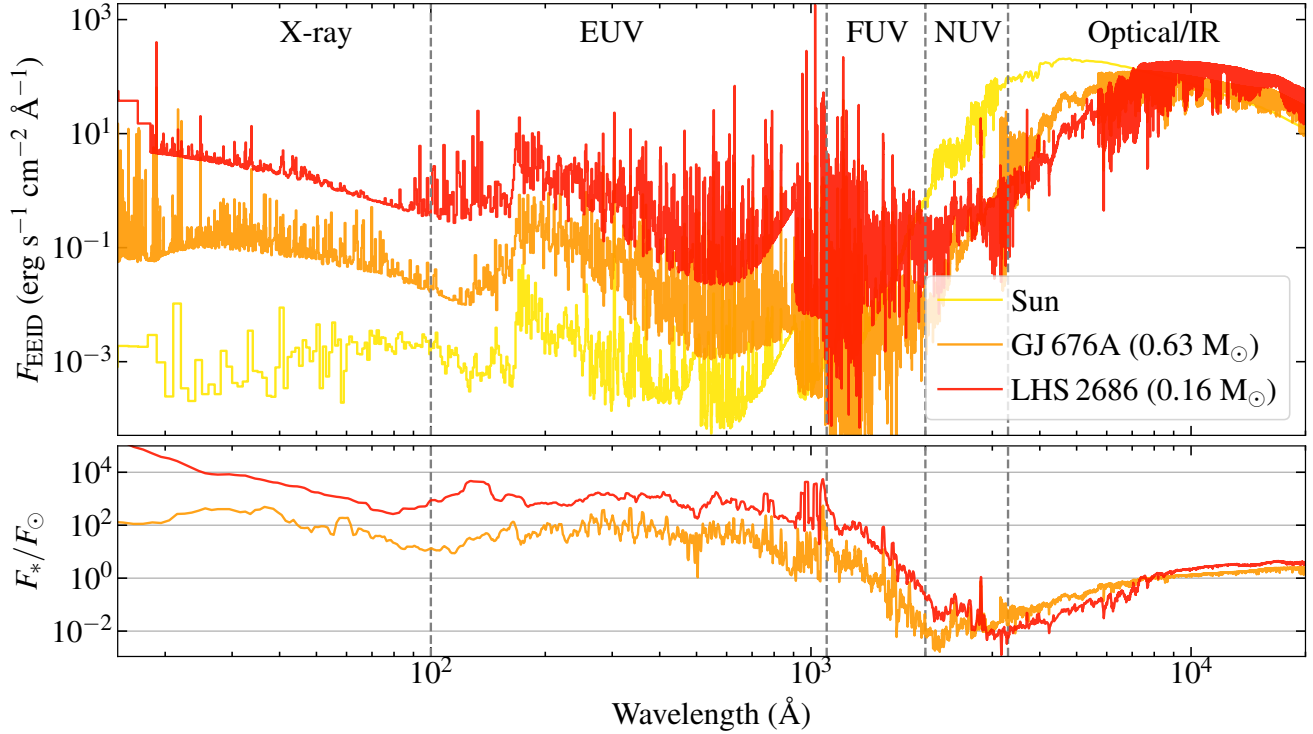


Figure 7. Top panel: SEDs of the hottest (GJ 676A) and second coolest (LHS 2686) compared with that of the Sun (Woods et al. 2009). The spectra are scaled to the Earth Equivalent Installation Distance (EEID, Mamajek & Stapelfeldt 2023). Bottom panel: The flux ratios of the scaled M dwarf SEDs to the Solar SED.

High-Level Science Product page hosted by MAST: <https://archive.stsci.edu/prepds/muscles/6>. The archive contains separate spectra for each instrument/grating combination, APEC, DEM, Lyman α and PHX models, as well as the combined SEDs. The SEDs are available in four different formats to provide for a range of user requirements:

- VAR-RES: The basic product, with all spectra and models included at their native resolutions. We recommend defaulting to this format for modelling.
- ADAPT-VAR-RES: This version down samples the observed spectra to remove negative flux points (which are a natural result of background subtraction from low S/N spectra). The spectrum is first divided into $\approx 10 \text{ \AA}$ chunks around prominent emission lines to avoid flux from emission lines being smeared out over a large wavelength range. Within each chunk, the most-negative flux bin and its two adjacent bins are replaced with the mean flux of all three, repeating until no negative bins remain. Whilst the overall flux is conserved, this does have the effect of smearing out smaller emission lines and can introduce a false continuum. We therefore recommend use of these spectra only when considering the integrated fluxes from large ($\gtrsim 100 \text{ \AA}$) wavelength ranges.
- CONST-RES and ADAPT-CONST-RES: As above, but the SEDs are rebinned to a resolution of 1 \AA using the SPECUTILS FLUX CONSERVING RESAMPLER routine (Carnall 2017). Rebinning is performed on the individual subspectra before combination into the SED to avoid combining fluxes from different sources into one bin. The native resolution of the PHOENIX models is less than 1 \AA at $\lambda > 1.3 \times 10^5 \text{ \AA}$, so bins red-ward of that are removed.

Our aim is that these four formats make the SEDs compatible inputs for as large as possible range of applications. If further custom formats are required please contact the corresponding author.

⁶ As the updated SEDs will not be available on MAST at the time of the arXiv upload of this paper, we have uploaded them here: <https://doi.org/10.5281/zenodo.14081035>

4. DISCUSSION

4.1. *M dwarfs as seen by their planets*

Figure 7 shows the SED of the Sun compared with the hottest and second coolest⁷ stars in our sample. The stellar spectra are scaled to the Earth-Equivalent Instellation Distance (EEID, Mamajek & Stapelfeldt 2023), i.e., the distance at which a planet receives the same total incident flux from the star as the Earth receives from the Sun. The bottom panel shows the ratio of the Solar SED to the Mdwarfs. It is clearly apparent that the high energy environment faced by M dwarf planets is radically different from that experienced by the Earth (Rugheimer et al. 2015b). The NUV fluxes are ~ 100 times lower but the FUV fluxes are similar, changing the inputs driving photochemical reactions in the upper atmospheres of planets. That is if the planets still have atmospheres: as the XUV fluxes are 100s to 1000s of times higher in M dwarf habitable zones than the Earth, planets there will be more susceptible to atmospheric escape (Zahnle & Catling 2017; Van Looveren et al. 2024). As continued JWST observations define the cosmic shoreline for M dwarf planets, XUV measurements will be vital for predicting and interpreting the presence or absence of atmospheres.

Figure 8 quantifies the differences in incident flux in the habitable zone for the entire sample, showing the flux in three wavebands at the EEID for the sample as a function of Rossby number. The Rossby number is the rotation period divided by the convective turnover time, and was calculated via the relationships given in Wright et al. (2018). The enhancement in EUV flux for planets around Mdwarfs is readily apparent, and will be even stronger for the closer-in planets that make up the bulk of currently accessible targets for transmission spectroscopy. It is likely that these planets experience significant atmospheric escape over their lifetimes, a conclusion thus far supported by JWST observation of rocky planets (e.g. Greene et al. 2023; Moran et al. 2023; Zieba et al. 2023) which have returned either ambiguous or clear non-detections of thick atmospheres. As atmospheric characterisation of habitable zone planets will take large investments of observing time (e.g. Wunderlich et al. 2020; Lin et al. 2021), careful modelling of atmospheric escape at these planets with our SEDs as input should be undertaken to establish if these planets can retain detectable atmospheres.

As found for multiple other activity tracers, most notably the X-ray luminosity (Wright et al. 2011, 2018; Brown et al. 2023), the ultraviolet fluxes follow a distinct trend with Rossby number: saturation below a certain critical Rossby number $Ro_{sat} \approx 0.1 - 0.2$ (Pineda et al. 2021a), then a power-law decline with higher Rossby number. Only two of our stars are below Ro_{sat} so we cannot confidently infer the flux values for saturation, but the decline above Ro_{sat} is clear. For a power-law decline $F_{HZ}/F_{Earth} = aRo^b$ we find:

$$\text{EUV : } a = 30 \pm 10, b = -1.4 \pm 0.6 \quad (R = 0.63)$$

$$\text{FUV : } a = 0.7 \pm 0.2, b = -1.4 \pm 0.5 \quad (R = 0.72)$$

$$\text{NUV : } a = 0.004 \pm 0.002, b = -1.3 \pm 0.6 \quad (R = 0.43)$$

With Pearson correlation coefficient R . Note is that the slope of the line is identical in all three bands. However there is considerable scatter around the best fit lines with large uncertainties on the fit coefficients, so we can only provide a rough approximation for the habitable zone high-energy fluxes around any given M dwarf: interpreting atmospheric observations ideally requires either direct observations of the host star as an input, or comparison of the SEDs of several stars with similar spectral types from this and other surveys. (Pineda et al. 2021a) carried out a similar experiment, fitting individual lines instead of integrated fluxes. They also found that the slope stayed roughly similar with wavelength, but was steeper, ($b \approx -2$ in our notation). With our small sample size and large uncertainties on the fits, it is unclear whether this is a true discrepancy or simple due to small number statistics.

4.2. *FUV to NUV flux ratio.*

In contrast to the absolute fluxes in the habitable zone, the ratios of the FUV to NUV fluxes of Mdwarfs follow a distinct trend. The FUV and NUV regions contain peaks in the photoionisation cross-sections of key molecules such as O_3 and CH_4 , and thus the detectable upper atmosphere chemistry of exoplanets will be shaped by the FUV/NUV input it receives from their host stars (Miguel et al. 2015). Figure 9 shows the ratios of the FUV to NUV fluxes for the Mega-MUSCLES and MUSCLES stars (Lloyd et al. 2016), plotted as a function of effective temperature. TRAPPIST-1 was excluded as the NUV signal from the spectra presented here is so weak that special treatment is required to

⁷ TRAPPIST-1 has already had a paper to itself (Wilson et al. 2021).

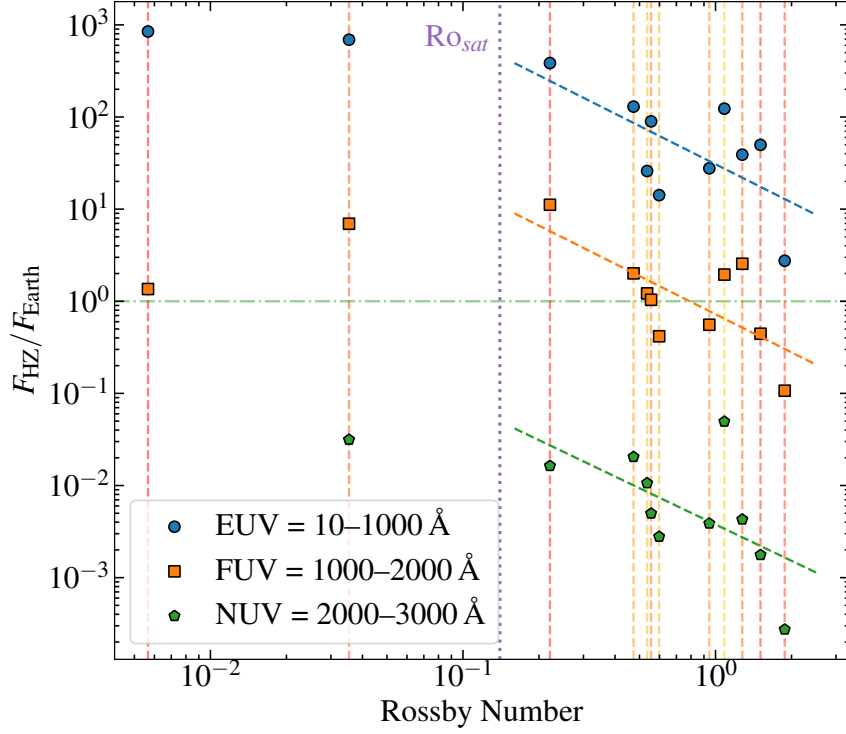


Figure 8. Integrated stellar fluxes for three wavelength ranges experienced in the center of the Habitable Zone for each star compared to the flux received at Earth, as a function of Rossby number. Vertical red/orange lines join the points for each star. Diagonal lines show the power law fits to the data at Rossby numbers higher than the critical Rossby number Ro_{sat} ($Ro_{\text{sat}} = 0.14$ from Wright et al. (2018)) is shown as a guide, the actual value is approximate and wavelength-dependant.)

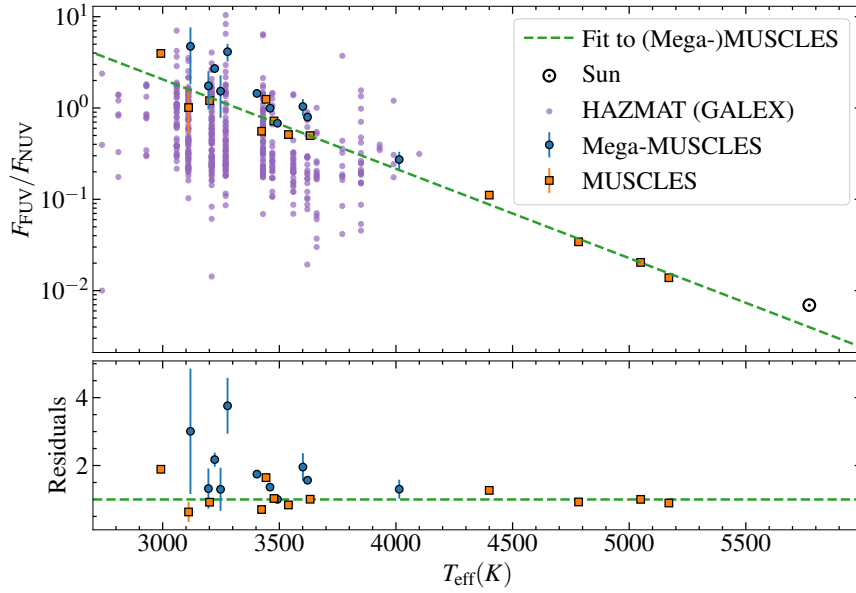


Figure 9. Ratio of the FUV to NUV flux as a function of stellar effective temperature. The bottom panel shows the observed ratios divided by those predicted by the linear fit. GALEX photometry from the HAZMAT project is shown in purple.

accurately account for the NUV flux (Peacock et al. 2019; Wilson et al. 2021), and additional NUV observations will be discussed elsewhere (Wilson et al. in prep). Effective temperatures were taken from Pineda et al. (2021b) and Loyd et al. (2016) for the M and K stars respectively. FUV and NUV fluxes were defined as the integral of the ranges 1000–2000 Å and 2000–3000 Å, with small changes in the ranges not affecting the result. As the MUSCLES SEDs do not contain uncertainty estimates for the Lyman α reconstruction or other models, we multiplied the uncertainty on the integrated fluxes by a factor 2 to better compare with the Mega-MUSCLES stars.

As with previous work (France et al. 2013; Behr et al. 2023), we find the FUV/NUV ratio falls with increasing effective temperature as the photospheric NUV flux increases. For the temperature range covered by our sample (≈ 3000 – 4000 K) we find that this trend is well fit with a simple linear relationship:

$$\log_{10}(F_{\text{FUV}}/F_{\text{NUV}}) = (-1 \pm 0.02) \times 10^{-3} T_{\text{eff}} + (3.3 \pm 0.1) \quad (R = 0.83) \quad (1)$$

The observed ratios are scattered around this line by factors of ≈ 0.6 – 3 (Figure 9, bottom panel). Whether or not this scatter matters for predictions of exoplanet atmospheric spectra may be an interesting future modelling project (Teal et al. 2022; Cooke et al. 2023). We also note that, in the range $T_{\text{eff}} \approx 3000$ – 4000 K, $F_{\text{FUV}}/F_{\text{NUV}} = 1$ is a reasonable approximation. The Solar FUV/NUV ratio, calculated using the spectrum from Woods et al. (2009), falls reasonably close to the line of best fit, although we caution against the use of this relationship for stars at spectral types earlier than K as this trend will turn over at higher temperatures due to increasing encroachment of the photosphere emission into the FUV. Further observations are required to define the FUV/NUV ratio across all spectral types of interest.

Ideally, spectroscopic observations are required. Figure 9 also shows the FUV/NUV ratios calculated from GALEX photometry as part of the HAZMAT survey (Schneider & Shkolnik 2018), with spectral type converted into temperature using the table from Pecaut & Mamajek (2013). Whilst they follow the same overall trend, the bulk of the HAZMAT stars fall under the relationship described by the spectroscopic observations. This is likely because the GALEX bands do not cover strong ultraviolet lines, especially Lyman α , so do not fully account for the stellar FUV and NUV fluxes that an orbiting exoplanet will experience. Whilst photometric observations from GALEX (or the upcoming UVEX mission, which will use similar filters) provide ultraviolet data for a vastly larger number of stars than can be practically obtained with spectroscopy, care must be taken to account for the missing emission features when applying the data to exoplanet atmosphere studies.

4.3. GJ 674 continuum

For the majority of the stars in our survey, the regions of the FUV spectra between strong emission lines have low S/N with flux values scattered around zero, i.e., at the noise floor of COS and STIS. The notable exception is GJ 674, where significant inter-line signal is detected in both COS G130M and STIS G140L spectra (Figure 10). The signal in the COS spectrum remains even when the contribution of the large flare described by Froning et al. (2019) is removed. The bottom panel of Figure 10 shows that the inter-line regions are actually a forest of small emission lines, but with underlying structure that is likely due to continuum emission from the stellar atmosphere. As with ϵ Eri (Loyd et al. 2016), there are hints of the Si II to Si I recombination edge between 1450 Å and 1550 Å. Unfortunately the range 1700–2250 Å is not detected in the STIS G230L observation, so we cannot provide a complete description of the stellar continuum across the entire ultraviolet range. However, the top panel of Figure 10 shows that the common treatment of the chromospheric continuum as a ≈ 8500 K blackbody (Ayres 1979; Peacock et al. 2019; Teal et al. 2022) significantly under predicts the stellar flux when extended into the FUV. Deep observations of bright M dwarfs coupled with semi-empirical models (Tilipman et al. 2021) are required to further understand the FUV continuum.

5. MEGA-MUSCLES SURVEY PAPERS

As noted in the introduction, there have been several prior publications on individual Mega-MUSCLES targets, as well as papers using the data for broader survey purposes. Here, we present a brief introduction to the publications, but refer the reader to the papers themselves for more details.

5.1. TRAPPIST-1

As a target of critical importance for exoplanetary science, production of the SED of TRAPPIST-1 was prioritised and released as described in Wilson et al. (2021). The Mega-MUSCLES TRAPPIST-1 SED remains mostly unchanged from that work, although a few small tweaks have been applied that improve the quality and usability of the high level science products, most notably the addition of uncertainties to the modelled regions of the spectrum.

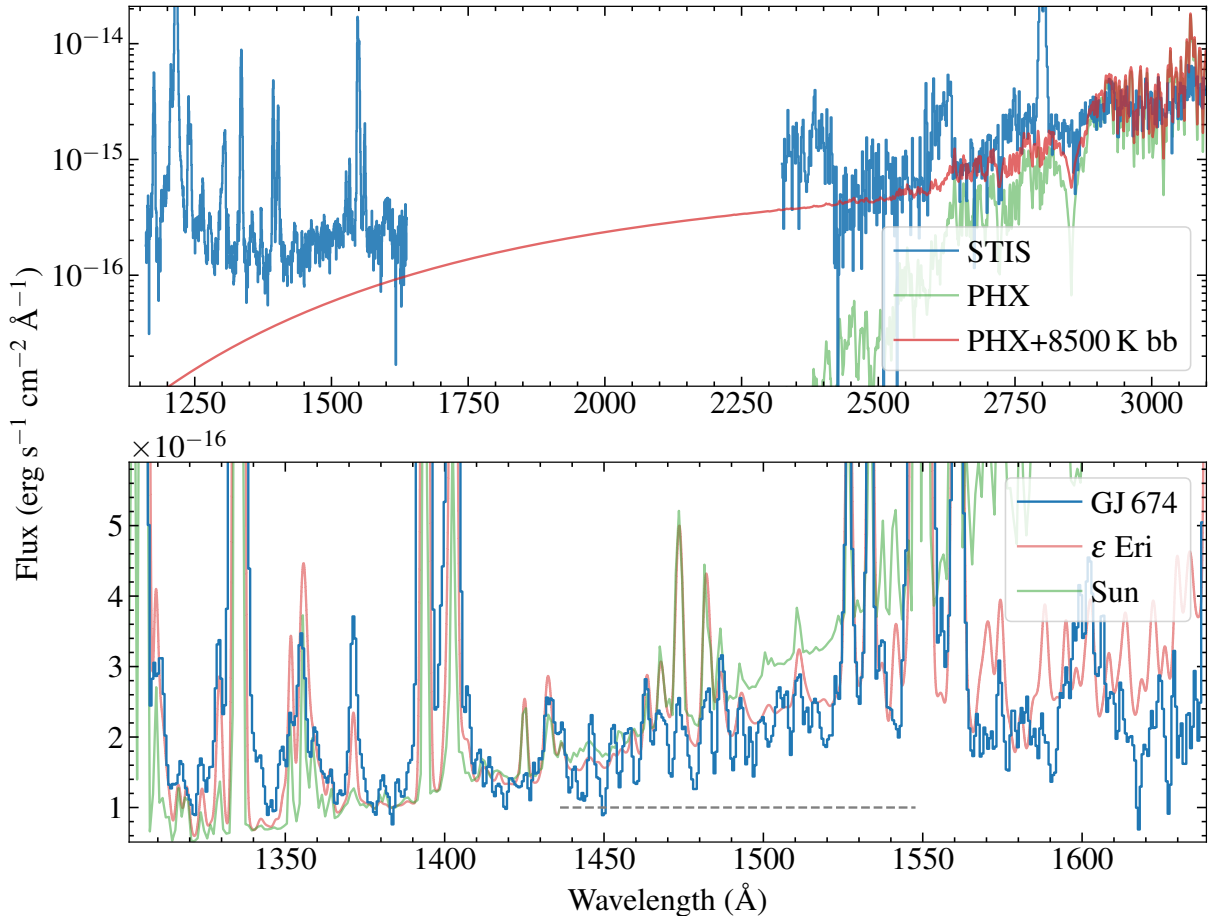


Figure 10. FUV continuum detection at GJ 674. Top panel: STIS G140L and G230L spectroscopy of GJ 674. The spectra are compared with the photospheric PHOENIX model used in the SED, and the PHOENIX model combined with a 8500 K blackbody. Bottom panel: GJ 674 compared with ϵ Eri and the Sun, scaled to have comparable fluxes in the region of interest and convolved to similar resolutions. The dashed line is included to aid the eye to see the potential Si recombination edge.

5.2. *GJ 674*

During the COS monitoring observations, the hot Neptune planet host GJ 674 exhibited a large stellar flare that persisted over an entire orbit. Although the absolute luminosity of the flare was not high, the equivalent duration was $> 30,000$ sec, comparable to the Great Flare observed on AD Leo (Hawley & Pettersen 1991). The FUV flare spectrum showed strong continuum emission that was well matched by a blackbody with a color temperature of $T_{br} \approx 40,000 \pm 10,000$ K, well in excess of typical 9000 K flare emission. Froning et al. (2019) presented the flare properties and compared them to parameterizations of radiative hydrodynamic models of chromospheric condensations in stellar flares. They showed that current flare models can only fit the observed continuum with the ad hoc addition of a hot, dense component in the chromospheric emission. The observation underscored the new information about stellar flare physics that is revealed as more ultraviolet observations of M stars are obtained.

5.3. *Barnard's Star*

Barnard's Star (GJ 699) has a 130 d rotation period and an estimated age of 10 or more Gyr (Toledo-Padrón et al. 2019). Despite its classification as an old M dwarf, it exhibited two ultraviolet flares and one X-ray flare during the Mega-MUSCLES observations, from which France et al. (2020) estimated a flare duty cycle of 25%. They used the flare and quiescent spectra to model the effects of the stellar radiation on a hypothetical terrestrial planet in the habitable

zone. The thermal and non-thermal escape models indicated that the quiescent flux was comparable to that seen by the Earth during solar active periods. However, the flare emission can drive significant hydrodynamic mass loss at the estimated duty cycle, suggesting that the recently discovered planet around Barnard’s Star (Gonzalez Hernandez et al. 2024), as well as exoplanets around old Mdwarfs in general, may still continue to risk significant atmospheric mass loss.

5.4. Survey Papers

The Mega-MUSCLES observations have been used in conjunction with other ultraviolet survey data in two publications. Linsky et al. (2020) used reconstructed Lyman α and X-ray observations from 79 stars to track correlations between stellar chromospheric and coronal emission, respectively. They find trends with stellar type and with age for the G–M sample. The M stars show systematically lower Lyman α emission at a given X-ray flux than the hotter stars. In addition, as stars age they show a smooth increase in normalized (to the bolometric luminosity) Lyman α luminosity to cooler stars at all ages; however, the increase in normalized X-ray coronal emission with decreasing effective temperature is much steeper than that of chromospheric emission in older stars. Thus, in M stars the relative rates of coronal and chromospheric emission vary with age differently than in hotter stars, indicative of changing distribution of heating that favors enhanced coronal emission in cooler stars.

Melbourne et al. (2020) also took advantage of the expanding archival observations of stellar ultraviolet emission to identify optical proxies to high energy emission in M stars. Using archival optical spectra, they examined relations between ultraviolet emission line fluxes and optical H α and Ca II H&K fluxes, conducting the analysis as a function of stellar temperature and age. They showed that the relation between ultraviolet line emission normalized to stellar bolometric luminosity and R'_{HK} can be used to predict the average ultraviolet emission from a M star in the absence of direct observation to within a factor of 2–4. On the other hand, the normalized ultraviolet luminosities showed no significant correlation with H α equivalent width.

Brown et al. (2023) presented the details of the X-ray observations used in both MUSCLES and Mega-MUSCLES. The data analysis process used is summarised in Sections 2.4 and 3.1. They found that the sample falls broadly on to the well-established relationship between X-ray luminosity and rotation (Wright et al. 2018), and that both short and long-term X-ray variability is common, particularly in low mass, fully convective stars.

6. SUMMARY

We have presented SEDs for twelve Mdwarfs, describing our observing strategy, model routines and methodology for each wavelength region. Combined with the original MUSCLES sample, Mega-MUSCLES provides the most comprehensive collection of M dwarf SEDs, covering a wide range of spectral types and ages. These data provide a vital input into interpretation of JWST observations of exoplanet atmospheres. Future observations will expand the SED library out to a wider range of spectral types, enabling exoplanet observations across the main sequence with current and future instrumentation.

ACKNOWLEDGMENTS

We thank the anonymous referee for comments that improved the manuscript.

Based on observations made with the NASA/ESA Hubble Space Telescope, obtained from the Data Archive at the Space Telescope Science Institute, which is operated by the Association of Universities for Research in Astronomy, Inc., under NASA contract NAS 5-26555. These observations are associated with program # 15071. Support for program #15071 was provided by NASA through a grant from the Space Telescope Science Institute, which is operated by the Association of Universities for Research in Astronomy, Inc., under NASA contract NAS 5-26555. All of the *HST* data presented in this paper were obtained from the Mikulski Archive for Space Telescopes (MAST).

This research has made use of data obtained from the Chandra Data Archive, and software provided by the Chandra X-ray Center (CXC) in the CIAO application package. This research has made use of data from *XMM-Newton*, an ESA science mission with instruments and contributions directly funded by ESA member states and NASA. This research has made use of data and/or software provided by the High Energy Astrophysics Science Archive Research Center (HEASARC), which is a service of the Astrophysics Science Division at NASA/GSFC. Support for X-ray analysis was provided by Chandra grant GO8-19017X.

This work has made use of data from the European Space Agency (ESA) mission *Gaia* (<https://www.cosmos.esa.int/gaia>), processed by the *Gaia* Data Processing and Analysis Consortium (DPAC, <https://www.cosmos.esa.int/web/gaia/dpac/consortium>). Funding for the DPAC has been provided by national institutions, in particular the institutions participating in the *Gaia* Multilateral Agreement.

This research has made use of the NASA Exoplanet Archive, which is operated by the California Institute of Technology, under contract with the National Aeronautics and Space Administration under the Exoplanet Exploration Program.

Y.M. acknowledges funding from the European Research Council (ERC) under the European Union’s Horizon 2020 research and innovation programme (grant agreement no. 101088557, N-GINE).

Facilities: *HST* (STIS and COS), *XMM-Newton*, *Chandra*

Software: *astropy* (Astropy Collaboration, 2018), *XSPEC* (Arnaud 1996), *stistools*⁸, *scipy* (Virtanen et al. 2020), *numpy* (Harris et al. 2020), *matplotlib* (Hunter 2007), *CHIANTI* (Dere et al. 1997; Del Zanna et al. 2021)

APPENDIX

A. ADDITIONAL TABLES

Here we provide full details of our ultraviolet and X-ray observations for each star (Table 4), line lists used to generate the DEMs (Table 5) and a summary of available archival data used to check the flux calibration of the G430L data (Table 6).

⁸ <https://stistools.readthedocs.io/en/latest/>

Table 4. Observation Summary

Star	HST Mode	Date	T_{exp} (sec)	X-ray mode	Date	T_{exp} (ksec)
GJ676A	COS G130M	2019-04-05	13015	Swift	2018-2019	6.7
	COS G230L	2019-04-05	333			
	STIS G140L	2019-04-01	12595			
	STIS G140M	2018-06-19	5500			
	STIS G230L	2018-06-19	3998			
	STIS G430L	2018-06-19	2			
GJ15A	STIS E140M	2019-02-13	9032	ACIS	2019-02-12	23.8
	STIS G230LB	2019-02-12	30			
	STIS G430L	2019-02-12	3			
	STIS E140M	2019-02-16	9032			
	STIS G230LB	2019-02-16	30			
	STIS G430L	2019-02-16	3			
GJ649	COS G130M	2018-03-04	12638	EPIC	2018-03-03	18
	COS G230L	2018-03-04	420			
	STIS G140L	2018-03-04	6408			
	STIS G140M	2018-03-04	3328			
	STIS G230L	2018-03-04	100			
	STIS G430L	2018-03-04	3			
GJ674	COS G130M	2018-04-03	12947	EPIC	2018-04-03	30.4
	COS G230L	2018-04-03	341			
	STIS G140L	2018-04-03	5486			
	STIS G140M	2018-04-03	3243			
	STIS G230L	2018-04-03	70			
	STIS G430L	2018-04-03	3			
GJ729	STIS E140M	2018-04-20	15200	EPIC	2019-03-04	23
	STIS G230LB	2018-04-19	80			
	STIS G430L	2018-04-19	30			
GJ163	COS G130M	2018-07-09	13133	ACIS	2019-30-14	28.6
	COS G160M	2018-07-08	10375			
	COS G230L	2018-07-09	2751			
	STIS G140M	2019-07-10	8251			
	STIS G230L	2019-07-10	1556			
	STIS G430L	2019-07-10	15			
GJ1132	COS G130M	2019-04-20	11757	EPIC	2019-01-10	46.6
	COS G160M	2019-04-17	6581			
	COS G230L	2019-04-17	5206			
	STIS G140M	2019-04-21	5202			
	STIS G230L	2019-04-21	4102			

Table 4 *continued on next page*

Table 4 (*continued*)

Star	HST Mode	Date	T_{exp} (sec)	X-ray mode	Date	T_{exp} (ksec)
	STIS G430L	2019-04-21	4			
L980-5	COS G130M	2019-03-15	12136	—	—	
	COS G160M	2019-03-13	9542			
	COS G230L	2019-30-13	2587			
	STIS G140M	2019-03-17	5172			
	STIS G230L	2019-03-17	4052			
	STIS G430L	2019-03-17	13			
GJ849	COS G130M	2019-06-09	12641	ACIS	2019-06-14	28
	COS G160M	2019-06-09	6807			
	COS G230L	2019-06-09	1011			
	STIS G140M	2019-06-09	500			
	STIS G230L	2019-06-09	154			
	STIS G430L	2019-06-09	3			
GJ699	COS G130M	2019-03-04	12902	ACIS	2019-06-17	26.7
	COS G230L	2019-03-04	331			
	STIS G140L	2019-03-04	7019			
	STIS G140M	2019-03-04	5933			
	STIS G230L	2019-03-04	205			
	STIS G430M	2019-03-04	5			
LHS2686	COS G130M	2019-05-31	13345	ACIS	2019-03-08	26.7
	STIS G140L	2019-06-01	5486			
	STIS G140M	2019-06-01	5482			
	STIS G230L	2019-06-01	1262			
	STIS G430L	2019-06-01	283			
	STIS G140L	2019-06-05	5486			
	STIS G140M	2019-06-05	5482			
	STIS G230L	2019-06-05	1262			
	STIS G430L	2019-06-05	283			
Trappist-1	COS G130M	2018-12-10	12404	EPIC	2018-12-10	24.6
	COS G160M	2019-06-07	1598			
	COS G230L	2017-12-15	2731			
	STIS G140M	2018-12-09	8131			
	STIS G430L	2018-12-09	1795			

^a Archival data from other programs.

Table 5. List of FUV emission line flux measurements used to create the DEMs. Lines marked “m” are multiplets where the given wavelength is the approximate midpoint.

Star	Line Flux (10^{-16} erg s $^{-1}$ cm $^{-2}$)										
	Si III	O V	N Vm	Fe XII	S II	Si II	C IIIm	Fe XXI	Si IVm	C IVm	
GJ 1132	1206.499 Å	1218.39 Å	1240.0 Å	1242.0 Å	1253.811 Å	1309.27 Å	1335.0 Å	1354.08 Å	1400.0 Å	1550.0 Å	
GJ 15A	0.21±0.01	...	0.25±0.12	0.63±0.03	...	0.07±0.01	1.23±0.87	
GJ 163	202.15±3.41	119.8±1.18	294.4±2.1	9.18±0.45	...	33.0±1.96	329 ± 3	...	208.10±6.15	1119.30±8.18	
GJ 649	6.91±2.00	0.44±0.03	0.63±0.02	< 1.6	1.95±0.04	<1.50	5.6 ± 0.28	0.70±0.04	
GJ 674	24.93±0.17	...	1.22 ± 0.3	...	44.36±0.17	<1.73	10 ± 5.0	65.56±3.28	
GJ 676A	77.80±0.37	...	121.14±0.52	4.9±0.16	0.87 ± 0.06	...	116.90±0.44	<0.17	
GJ 699	...	5.25±0.53	48.05±0.23	72.10±7.21	<1.03	14.6 ± 1.5	88.44±8.84	
GJ 729	14.39±1.25	...	31.49±0.61	0.7±0.06	0.02±0.16	0.35±0.06	50.65±1.25	<0.24	
GJ 849	28.98±1.50	7.50±0.69	34.66±0.67	...	1.94 ± 0.8	65.59±2.08	
GJ 876	<0.27	5.97±0.06	44.81±0.21	44.73±0.09	...	22.5 ± 0.5	33.26±0.39	
L-980-5	27.62±2.67	17.38±1.60	47.12±4.03	0.7±0.07	0.37 ± 0.06	...	56.41±5.59	...	8.3±0.8	158.88±12.01	
LHS-2686	0.77±0.05	<1.03	0.87±0.06	0.98±0.02	...	1.4 ± 0.03	6.30±4.52	
TRAPPIST-1	7.17±0.09	...	22.26±0.23	16.05±0.20	
	0.52±0.12	0.06±0.03	0.39 ± 0.2	1.53±0.49	

Name	CASLEO	X-shooter
TRAPPIST-1	N	N
L-980-5	N	N
GJ674	Y	N
GJ676A	N	Y
GJ649	N	N
GJ699	Y	N
GJ163	N	Y
GJ849	N	Y
GJ1132	N	N
LHS-2686	N	N
GJ729	Y	Y
GJ15A	N	N

Table 6. Ground based optical spectra used to assess the flux calibration of the G430L spectra.

REFERENCES

- Allard, F. 2016, in SF2A-2016: Proceedings of the Annual meeting of the French Society of Astronomy and Astrophysics, ed. C. Reyl  , J. Richard, L. Cambr  sy, M. Deleuil, E. P  contal, L. Tresse, & I. Vauglin, 223–227
- Allen, C., & Herrera, M. A. 1998, *RMxAA*, 34, 37
- Anglada-Escud  , G., & Tuomi, M. 2012, *A&A*, 548, A58, doi: [10.1051/0004-6361/201219910](https://doi.org/10.1051/0004-6361/201219910)
- Anglada-Escud  , G., Amado, P. J., Barnes, J., et al. 2016, *Nature*, 536, 437, doi: [10.1038/nature19106](https://doi.org/10.1038/nature19106)
- Arnaud, K. A. 1996, in *Astronomical Society of the Pacific Conference Series*, Vol. 101, *Astronomical Data Analysis Software and Systems V*, ed. G. H. Jacoby & J. Barnes, 17
- Astropy Collaboration, Price-Whelan, A. M., Sip  cz, B. M., et al. 2018, *AJ*, 156, 123, doi: [10.3847/1538-3881/aabc4f](https://doi.org/10.3847/1538-3881/aabc4f)
- Ayres, T. R. 1979, *ApJ*, 228, 509, doi: [10.1086/156873](https://doi.org/10.1086/156873)
- Baraffe, I., Homeier, D., Allard, F., & Chabrier, G. 2015, *A&A*, 577, A42, doi: [10.1051/0004-6361/201425481](https://doi.org/10.1051/0004-6361/201425481)
- Behr, P. R., France, K., Brown, A., et al. 2023, *AJ*, 166, 35, doi: [10.3847/1538-3881/acdb70](https://doi.org/10.3847/1538-3881/acdb70)
- Berta-Thompson, Z. K., Irwin, J., Charbonneau, D., et al. 2015, *Nature*, 527, 204, doi: [10.1038/nature15762](https://doi.org/10.1038/nature15762)
- Bonfils, X., Mayor, M., Delfosse, X., et al. 2007, *A&A*, 474, 293, doi: [10.1051/0004-6361:20077068](https://doi.org/10.1051/0004-6361:20077068)
- Bonfils, X., Lo Curto, G., Correia, A. C. M., et al. 2013, *A&A*, 556, A110, doi: [10.1051/0004-6361/201220237](https://doi.org/10.1051/0004-6361/201220237)
- Bonfils, X., Almenara, J. M., Cloutier, R., et al. 2018, *A&A*, 618, A142, doi: [10.1051/0004-6361/201731884](https://doi.org/10.1051/0004-6361/201731884)
- Bourrier, V., Ehrenreich, D., Wheatley, P. J., et al. 2017, *A&A*, 599, L3, doi: [10.1051/0004-6361/201630238](https://doi.org/10.1051/0004-6361/201630238)
- Brown, A., Schneider, P. C., France, K., et al. 2023, *AJ*, 165, 195, doi: [10.3847/1538-3881/acc38a](https://doi.org/10.3847/1538-3881/acc38a)
- Buccino, A. P., Lemarchand, G. A., & Mauas, P. J. D. 2007, *Icarus*, 192, 582, doi: [10.1016/j.icarus.2007.08.012](https://doi.org/10.1016/j.icarus.2007.08.012)
- Burgasser, A. J., & Mamajek, E. E. 2017, *ApJ*, 845, 110, doi: [10.3847/1538-4357/aa7fea](https://doi.org/10.3847/1538-4357/aa7fea)
- Butler, R. P., Johnson, J. A., Marcy, G. W., et al. 2006, *PASP*, 118, 1685, doi: [10.1086/510500](https://doi.org/10.1086/510500)
- Carnall, A. C. 2017, arXiv e-prints, arXiv:1705.05165, doi: [10.48550/arXiv.1705.05165](https://doi.org/10.48550/arXiv.1705.05165)
- Cooke, G. J., Marsh, D. R., Walsh, C., & Youngblood, A. 2023, *ApJ*, 959, 45, doi: [10.3847/1538-4357/ad0381](https://doi.org/10.3847/1538-4357/ad0381)
- Del Zanna, G., Dere, K. P., Young, P. R., & Landi, E. 2021, *ApJ*, 909, 38, doi: [10.3847/1538-4357/abd8ce](https://doi.org/10.3847/1538-4357/abd8ce)
- Dere, K. P., Landi, E., Mason, H. E., Monsignori Fossi, B. C., & Young, P. R. 1997, *A&AS*, 125, 149, doi: [10.1051/aas:1997368](https://doi.org/10.1051/aas:1997368)
- Diamond-Lowe, H., Kreidberg, L., Harman, C. E., et al. 2022, *AJ*, 164, 172, doi: [10.3847/1538-3881/ac7807](https://doi.org/10.3847/1538-3881/ac7807)
- D  ez Alonso, E., Gonz  lez Hern  ndez, J. I., Toledo-Padr  n, B., et al. 2019, *MNRAS*, 489, 5928, doi: [10.1093/mnras/sty3467](https://doi.org/10.1093/mnras/sty3467)
- Dittmann, J. A., Irwin, J. M., Charbonneau, D., et al. 2017, *Nature*, 544, 333, doi: [10.1038/nature22055](https://doi.org/10.1038/nature22055)
- Duvvuri, G. M., Cauley, P. W., Aguirre, F. C., et al. 2023, *AJ*, 166, 196, doi: [10.3847/1538-3881/acfa74](https://doi.org/10.3847/1538-3881/acfa74)
- Duvvuri, G. M., Sebastian Pineda, J., Berta-Thompson, Z. K., et al. 2021, *ApJ*, 913, 40, doi: [10.3847/1538-4357/abeaaf](https://doi.org/10.3847/1538-4357/abeaaf)
- Feinstein, A. D., France, K., Youngblood, A., et al. 2022, *AJ*, 164, 110, doi: [10.3847/1538-3881/ac8107](https://doi.org/10.3847/1538-3881/ac8107)
- Fontenla, J. M., Stancil, P. C., & Landi, E. 2015, *ApJ*, 809, 157, doi: [10.1088/0004-637X/809/2/157](https://doi.org/10.1088/0004-637X/809/2/157)
- Foreman-Mackey, D., Hogg, D. W., Lang, D., & Goodman, J. 2013, *PASP*, 125, 306, doi: [10.1086/670067](https://doi.org/10.1086/670067)

- Fortenbach, C. D., & Dressing, C. D. 2020, *PASP*, 132, 054501, doi: [10.1088/1538-3873/ab70da](https://doi.org/10.1088/1538-3873/ab70da)
- Foster, A. R., Ji, L., Smith, R. K., & Brickhouse, N. S. 2012, *ApJ*, 756, 128, doi: [10.1088/0004-637X/756/2/128](https://doi.org/10.1088/0004-637X/756/2/128)
- France, K., Froning, C. S., Linsky, J. L., et al. 2013, *ApJ*, 763, 149, doi: [10.1088/0004-637X/763/2/149](https://doi.org/10.1088/0004-637X/763/2/149)
- France, K., Loyd, R. O. P., Youngblood, A., et al. 2016, *ApJ*, 820, 89, doi: [10.3847/0004-637X/820/2/89](https://doi.org/10.3847/0004-637X/820/2/89)
- France, K., Duvvuri, G., Egan, H., et al. 2020, *AJ*, 160, 237, doi: [10.3847/1538-3881/abb465](https://doi.org/10.3847/1538-3881/abb465)
- Froning, C. S., Kowalski, A., France, K., et al. 2019, *ApJL*, 871, L26, doi: [10.3847/2041-8213/aaffcd](https://doi.org/10.3847/2041-8213/aaffcd)
- Gaia Collaboration, Prusti, T., de Bruijne, J. H. J., et al. 2016, *A&A*, 595, A1, doi: [10.1051/0004-6361/201629272](https://doi.org/10.1051/0004-6361/201629272)
- Gaia Collaboration, Brown, A. G. A., Vallenari, A., et al. 2018, *A&A*, 616, A1, doi: [10.1051/0004-6361/201833051](https://doi.org/10.1051/0004-6361/201833051)
- Gillon, M., Jehin, E., Lederer, S. M., et al. 2016, *Nature*, 533, 221, doi: [10.1038/nature17448](https://doi.org/10.1038/nature17448)
- Gillon, M., Triaud, A. H. M. J., Demory, B.-O., et al. 2017, *Nature*, 542, 456, doi: [10.1038/nature21360](https://doi.org/10.1038/nature21360)
- Gonzalez Hernandez, J. I., Suarez Mascareno, A., Silva, A. M., et al. 2024, arXiv e-prints, arXiv:2410.00569, doi: [10.48550/arXiv.2410.00569](https://doi.org/10.48550/arXiv.2410.00569)
- Green, J. C., Froning, C. S., Osterman, S., et al. 2012, *ApJ*, 744, 60, doi: [10.1088/0004-637X/744/1/60](https://doi.org/10.1088/0004-637X/744/1/60)
- Greene, T. P., Bell, T. J., Ducrot, E., et al. 2023, *Nature*, 618, 39, doi: [10.1038/s41586-023-05951-7](https://doi.org/10.1038/s41586-023-05951-7)
- Grimm, S. L., Demory, B.-O., Gillon, M., et al. 2018, *A&A*, 613, A68, doi: [10.1051/0004-6361/201732233](https://doi.org/10.1051/0004-6361/201732233)
- Guinan, E. F., Engle, S. G., & Durbin, A. 2016, *ApJ*, 821, 81, doi: [10.3847/0004-637X/821/2/81](https://doi.org/10.3847/0004-637X/821/2/81)
- Harris, C. R., Millman, K. J., van der Walt, S. J., et al. 2020, *Nature*, 585, 357, doi: [10.1038/s41586-020-2649-2](https://doi.org/10.1038/s41586-020-2649-2)
- Hawley, S. L., & Pettersen, B. R. 1991, *ApJ*, 378, 725, doi: [10.1086/170474](https://doi.org/10.1086/170474)
- Henry, T. J., Jao, W.-C., Subasavage, J. P., et al. 2006, *AJ*, 132, 2360, doi: [10.1086/508233](https://doi.org/10.1086/508233)
- Howard, A. W., Marcy, G. W., Fischer, D. A., et al. 2014, *ApJ*, 794, 51, doi: [10.1088/0004-637X/794/1/51](https://doi.org/10.1088/0004-637X/794/1/51)
- Hunter, J. D. 2007, *Computing in Science & Engineering*, 9, 90, doi: [10.1109/MCSE.2007.55](https://doi.org/10.1109/MCSE.2007.55)
- Husser, T. O., Wende-von Berg, S., Dreizler, S., et al. 2013, *A&A*, 553, A6, doi: [10.1051/0004-6361/201219058](https://doi.org/10.1051/0004-6361/201219058)
- Ibañez Bustos, R. V., Buccino, A. P., Messina, S., Lanza, A. F., & Mauas, P. J. D. 2020, *A&A*, 644, A2, doi: [10.1051/0004-6361/202039164](https://doi.org/10.1051/0004-6361/202039164)
- Johnson, J. A., Aller, K. M., Howard, A. W., & Crepp, J. R. 2010, *PASP*, 122, 905, doi: [10.1086/655775](https://doi.org/10.1086/655775)
- JWST Transiting Exoplanet Community Early Release Science Team, Ahrer, E.-M., Alderson, L., et al. 2023, *Nature*, 614, 649, doi: [10.1038/s41586-022-05269-w](https://doi.org/10.1038/s41586-022-05269-w)
- Kamgar, L., France, K., & Youngblood, A. 2024, *PASP*, 136, 024202, doi: [10.1088/1538-3873/ad119f](https://doi.org/10.1088/1538-3873/ad119f)
- Kawashima, Y., Hu, R., & Ikoma, M. 2019, *ApJL*, 876, L5, doi: [10.3847/2041-8213/ab16f6](https://doi.org/10.3847/2041-8213/ab16f6)
- Kempton, E. M. R., Bean, J. L., Louie, D. R., et al. 2018, *PASP*, 130, 114401, doi: [10.1088/1538-3873/aadf6f](https://doi.org/10.1088/1538-3873/aadf6f)
- Kiraga, M., & Stepien, K. 2007, *AcA*, 57, 149, <https://arxiv.org/abs/0707.2577>
- Kopparapu, R. K., Ramirez, R. M., SchottelKotte, J., et al. 2014, *ApJL*, 787, L29, doi: [10.1088/2041-8205/787/2/L29](https://doi.org/10.1088/2041-8205/787/2/L29)
- Lin, Z., MacDonald, R. J., Kaltenecker, L., & Wilson, D. J. 2021, *MNRAS*, 505, 3562, doi: [10.1093/mnras/stab1486](https://doi.org/10.1093/mnras/stab1486)
- Lincowski, A. P., Meadows, V. S., Zieba, S., et al. 2023, arXiv e-prints, arXiv:2308.05899, doi: [10.48550/arXiv.2308.05899](https://doi.org/10.48550/arXiv.2308.05899)
- Linsky, J. L., Fontenla, J., & France, K. 2014, *ApJ*, 780, 61, doi: [10.1088/0004-637X/780/1/61](https://doi.org/10.1088/0004-637X/780/1/61)
- Linsky, J. L., Wood, B. E., Youngblood, A., et al. 2020, *ApJ*, 902, 3, doi: [10.3847/1538-4357/abb36f](https://doi.org/10.3847/1538-4357/abb36f)
- Louca, A. J., Miguel, Y., Tsai, S.-M., et al. 2023, *MNRAS*, 521, 3333, doi: [10.1093/mnras/stac1220](https://doi.org/10.1093/mnras/stac1220)
- Loyd, R. O. P., Shkolnik, E. L., Schneider, A. C., et al. 2018a, *ApJ*, 867, 70, doi: [10.3847/1538-4357/aae2ae](https://doi.org/10.3847/1538-4357/aae2ae)
- Loyd, R. O. P., France, K., Youngblood, A., et al. 2016, *ApJ*, 824, 102, doi: [10.3847/0004-637X/824/2/102](https://doi.org/10.3847/0004-637X/824/2/102)
- . 2018b, *ApJ*, 867, 71, doi: [10.3847/1538-4357/aae2bd](https://doi.org/10.3847/1538-4357/aae2bd)
- Loyd, R. O. P., Shkolnik, E. L., Schneider, A. C., et al. 2021, *ApJ*, 907, 91, doi: [10.3847/1538-4357/abd0f0](https://doi.org/10.3847/1538-4357/abd0f0)
- Loyd, R. O. P., Schneider, P. C., Jackman, J. A. G., et al. 2023, *AJ*, 165, 146, doi: [10.3847/1538-3881/acbbc8](https://doi.org/10.3847/1538-3881/acbbc8)
- MacGregor, M. A., Weinberger, A. J., Loyd, R. O. P., et al. 2021, *ApJL*, 911, L25, doi: [10.3847/2041-8213/abf14c](https://doi.org/10.3847/2041-8213/abf14c)
- Mamajek, E., & Stapelfeldt, K. 2023, in *American Astronomical Society Meeting Abstracts*, Vol. 55, *American Astronomical Society Meeting Abstracts*, 116.07
- Mann, A. W., Feiden, G. A., Gaidos, E., Boyajian, T., & von Braun, K. 2015, *ApJ*, 804, 64, doi: [10.1088/0004-637X/804/1/64](https://doi.org/10.1088/0004-637X/804/1/64)
- Mann, A. W., Dupuy, T., Kraus, A. L., et al. 2019, *ApJ*, 871, 63, doi: [10.3847/1538-4357/aaf3bc](https://doi.org/10.3847/1538-4357/aaf3bc)
- Mariska, J. T. 1992, *The Solar Transition Region*
- Melbourne, K., Youngblood, A., France, K., et al. 2020, *AJ*, 160, 269, doi: [10.3847/1538-3881/abfb5c](https://doi.org/10.3847/1538-3881/abfb5c)
- Miguel, Y., Kaltenecker, L., Linsky, J. L., & Rugheimer, S. 2015, *MNRAS*, 446, 345, doi: [10.1093/mnras/stu2107](https://doi.org/10.1093/mnras/stu2107)

- Montes, D., López-Santiago, J., Gálvez, M. C., et al. 2001, *MNRAS*, 328, 45, doi: [10.1046/j.1365-8711.2001.04781.x](https://doi.org/10.1046/j.1365-8711.2001.04781.x)
- Montet, B. T., Crepp, J. R., Johnson, J. A., Howard, A. W., & Marcy, G. W. 2014, *ApJ*, 781, 28, doi: [10.1088/0004-637X/781/1/28](https://doi.org/10.1088/0004-637X/781/1/28)
- Moran, S. E., Stevenson, K. B., Sing, D. K., et al. 2023, *ApJL*, 948, L11, doi: [10.3847/2041-8213/accb9c](https://doi.org/10.3847/2041-8213/accb9c)
- Morley, C. V., Kreidberg, L., Rustamkulov, Z., Robinson, T., & Fortney, J. J. 2017, *ApJ*, 850, 121, doi: [10.3847/1538-4357/aa927b](https://doi.org/10.3847/1538-4357/aa927b)
- Moses, J. I., Line, M. R., Visscher, C., et al. 2013, *ApJ*, 777, 34, doi: [10.1088/0004-637X/777/1/34](https://doi.org/10.1088/0004-637X/777/1/34)
- Newton, E. R., Irwin, J., Charbonneau, D., et al. 2017, *ApJ*, 834, 85, doi: [10.3847/1538-4357/834/1/85](https://doi.org/10.3847/1538-4357/834/1/85)
- Newton, E. R., Irwin, J., Charbonneau, D., Berta-Thompson, Z. K., & Dittmann, J. A. 2016, *ApJL*, 821, L19, doi: [10.3847/2041-8205/821/1/L19](https://doi.org/10.3847/2041-8205/821/1/L19)
- Newton, E. R., Mondrik, N., Irwin, J., Winters, J. G., & Charbonneau, D. 2018, *AJ*, 156, 217, doi: [10.3847/1538-3881/aad73b](https://doi.org/10.3847/1538-3881/aad73b)
- Peacock, S., Barman, T., Shkolnik, E. L., Hauschildt, P. H., & Baron, E. 2019, *ApJ*, 871, 235, doi: [10.3847/1538-4357/aaf891](https://doi.org/10.3847/1538-4357/aaf891)
- Pecaut, M. J., & Mamajek, E. E. 2013, *ApJS*, 208, 9, doi: [10.1088/0067-0049/208/1/9](https://doi.org/10.1088/0067-0049/208/1/9)
- Peralta, J. I., Vieytes, M. C., Mendez, A. M. P., & Mitnik, D. M. 2023, *A&A*, 676, A18, doi: [10.1051/0004-6361/202346156](https://doi.org/10.1051/0004-6361/202346156)
- Pidhorodetska, D., Moran, S. E., Schwieterman, E. W., et al. 2021, *AJ*, 162, 169, doi: [10.3847/1538-3881/ac1171](https://doi.org/10.3847/1538-3881/ac1171)
- Pineda, J. S., Youngblood, A., & France, K. 2021a, *ApJ*, 911, 111, doi: [10.3847/1538-4357/abe8d7](https://doi.org/10.3847/1538-4357/abe8d7)
- . 2021b, arXiv e-prints, arXiv:2106.07656. <https://arxiv.org/abs/2106.07656>
- Poppenhaeger, K., Ketzner, L., Ilic, N., et al. 2024, arXiv e-prints, arXiv:2401.17302, doi: [10.48550/arXiv.2401.17302](https://doi.org/10.48550/arXiv.2401.17302)
- Redfield, S., & Linsky, J. L. 2008, *ApJ*, 673, 283, doi: [10.1086/524002](https://doi.org/10.1086/524002)
- Redfield, S., Batalha, N., Benneke, B., et al. 2024, arXiv e-prints, arXiv:2404.02932, doi: [10.48550/arXiv.2404.02932](https://doi.org/10.48550/arXiv.2404.02932)
- Ribas, I., Tuomi, M., Reiners, A., et al. 2018, *Nature*, 563, 365, doi: [10.1038/s41586-018-0677-y](https://doi.org/10.1038/s41586-018-0677-y)
- Rockcliffe, K. E., Newton, E. R., Youngblood, A., et al. 2021, *AJ*, 162, 116, doi: [10.3847/1538-3881/ac126f](https://doi.org/10.3847/1538-3881/ac126f)
- Rosenthal, L. J., Fulton, B. J., Hirsch, L. A., et al. 2021, *ApJS*, 255, 8, doi: [10.3847/1538-4365/abe23c](https://doi.org/10.3847/1538-4365/abe23c)
- Rugheimer, S., & Kaltenegger, L. 2018, *ApJ*, 854, 19, doi: [10.3847/1538-4357/aaa47a](https://doi.org/10.3847/1538-4357/aaa47a)
- Rugheimer, S., Kaltenegger, L., Segura, A., Linsky, J., & Mohanty, S. 2015a, *ApJ*, 809, 57, doi: [10.1088/0004-637X/809/1/57](https://doi.org/10.1088/0004-637X/809/1/57)
- Rugheimer, S., Segura, A., Kaltenegger, L., & Sasselov, D. 2015b, *ApJ*, 806, 137, doi: [10.1088/0004-637X/806/1/137](https://doi.org/10.1088/0004-637X/806/1/137)
- Sahlmann, J., Lazorenko, P. F., Ségransan, D., et al. 2016, *A&A*, 595, A77, doi: [10.1051/0004-6361/201628854](https://doi.org/10.1051/0004-6361/201628854)
- Schneider, A. C., & Shkolnik, E. L. 2018, *AJ*, 155, 122, doi: [10.3847/1538-3881/aaaa24](https://doi.org/10.3847/1538-3881/aaaa24)
- Segura, A., Kasting, J. F., Meadows, V., et al. 2005, *Astrobiology*, 5, 706, doi: [10.1089/ast.2005.5.706](https://doi.org/10.1089/ast.2005.5.706)
- Smith, R. K., Brickhouse, N. S., Liedahl, D. A., & Raymond, J. C. 2001, *ApJ*, 556, L91, doi: [10.1086/322992](https://doi.org/10.1086/322992)
- Spake, J. J., Sing, D. K., Evans, T. M., et al. 2018, *Nature*, 557, 68, doi: [10.1038/s41586-018-0067-5](https://doi.org/10.1038/s41586-018-0067-5)
- Suárez Mascareño, A., Rebolo, R., González Hernández, J. I., & Esposito, M. 2015, *MNRAS*, 452, 2745, doi: [10.1093/mnras/stv1441](https://doi.org/10.1093/mnras/stv1441)
- Tarter, J. C., Backus, P. R., Mancinelli, R. L., et al. 2007, *Astrobiology*, 7, 30, doi: [10.1089/ast.2006.0124](https://doi.org/10.1089/ast.2006.0124)
- Teal, D. J., Kempton, E. M. R., Bastelberger, S., Youngblood, A., & Arney, G. 2022, *ApJ*, 927, 90, doi: [10.3847/1538-4357/ac4d99](https://doi.org/10.3847/1538-4357/ac4d99)
- Tilipman, D., Vieytes, M., Linsky, J. L., Buccino, A. P., & France, K. 2021, *ApJ*, 909, 61, doi: [10.3847/1538-4357/abd62f](https://doi.org/10.3847/1538-4357/abd62f)
- Toledo-Padrón, B., González Hernández, J. I., Rodríguez-López, C., et al. 2019, *MNRAS*, 488, 5145, doi: [10.1093/mnras/stz1975](https://doi.org/10.1093/mnras/stz1975)
- Van Looveren, G., Güdel, M., Boro Saikia, S., & Kislyakova, K. 2024, *A&A*, 683, A153, doi: [10.1051/0004-6361/202348079](https://doi.org/10.1051/0004-6361/202348079)
- Veyette, M. J., & Muirhead, P. S. 2018, *ApJ*, 863, 166, doi: [10.3847/1538-4357/aad40e](https://doi.org/10.3847/1538-4357/aad40e)
- Vida, K., Kővári, Z., Pál, A., Oláh, K., & Kriskovics, L. 2017, *ApJ*, 841, 124, doi: [10.3847/1538-4357/aa6f05](https://doi.org/10.3847/1538-4357/aa6f05)
- Virtanen, P., Gommers, R., Oliphant, T. E., et al. 2020, *Nature Methods*, 17, 261, doi: [10.1038/s41592-019-0686-2](https://doi.org/10.1038/s41592-019-0686-2)
- Waalkes, W. C., Berta-Thompson, Z., Bourrier, V., et al. 2019, *AJ*, 158, 50, doi: [10.3847/1538-3881/ab24c2](https://doi.org/10.3847/1538-3881/ab24c2)
- Watson, A. J., Donahue, T. M., & Walker, J. C. G. 1981, *Icarus*, 48, 150, doi: [10.1016/0019-1035\(81\)90101-9](https://doi.org/10.1016/0019-1035(81)90101-9)
- Wheatley, P. J., Loudon, T., Bourrier, V., Ehrenreich, D., & Gillon, M. 2017, *MNRAS*, 465, L74, doi: [10.1093/mnrasl/slz192](https://doi.org/10.1093/mnrasl/slz192)
- Wilson, D. J., Froning, C. S., Duvvuri, G. M., et al. 2021, *ApJ*, 911, 18, doi: [10.3847/1538-4357/abe771](https://doi.org/10.3847/1538-4357/abe771)
- Wilson, D. J., Youngblood, A., Toloza, O., et al. 2022, *ApJ*, 936, 189, doi: [10.3847/1538-4357/ac87a8](https://doi.org/10.3847/1538-4357/ac87a8)

- Winters, J. G., Medina, A. A., Irwin, J. M., et al. 2019, *AJ*, 158, 152, doi: [10.3847/1538-3881/ab364d](https://doi.org/10.3847/1538-3881/ab364d)
- Woodgate, B. E., Kimble, R. A., Bowers, C. W., et al. 1998, *PASP*, 110, 1183, doi: [10.1086/316243](https://doi.org/10.1086/316243)
- Woods, T. N., Chamberlin, P. C., Harder, J. W., et al. 2009, *Geophys. Res. Lett.*, 36, L01101, doi: [10.1029/2008GL036373](https://doi.org/10.1029/2008GL036373)
- Wright, N. J., Drake, J. J., Mamajek, E. E., & Henry, G. W. 2011, *ApJ*, 743, 48, doi: [10.1088/0004-637X/743/1/48](https://doi.org/10.1088/0004-637X/743/1/48)
- Wright, N. J., Newton, E. R., Williams, P. K. G., Drake, J. J., & Yadav, R. K. 2018, *MNRAS*, 479, 2351, doi: [10.1093/mnras/sty1670](https://doi.org/10.1093/mnras/sty1670)
- Wunderlich, F., Scheucher, M., Godolt, M., et al. 2020, *ApJ*, 901, 126, doi: [10.3847/1538-4357/aba59c](https://doi.org/10.3847/1538-4357/aba59c)
- Youngblood, A., Pineda, J. S., Ayres, T., et al. 2022, *ApJ*, 926, 129, doi: [10.3847/1538-4357/ac4711](https://doi.org/10.3847/1538-4357/ac4711)
- Youngblood, A., Pineda, J. S., & France, K. 2021, *ApJ*, 911, 112, doi: [10.3847/1538-4357/abe8d8](https://doi.org/10.3847/1538-4357/abe8d8)
- Youngblood, A., France, K., Loyd, R. O. P., et al. 2016, *ApJ*, 824, 101, doi: [10.3847/0004-637X/824/2/101](https://doi.org/10.3847/0004-637X/824/2/101)
- . 2017, *ApJ*, 843, 31, doi: [10.3847/1538-4357/aa76dd](https://doi.org/10.3847/1538-4357/aa76dd)
- Zahnle, K. J., & Catling, D. C. 2017, *ApJ*, 843, 122, doi: [10.3847/1538-4357/aa7846](https://doi.org/10.3847/1538-4357/aa7846)
- Zieba, S., Kreidberg, L., Ducrot, E., et al. 2023, *arXiv e-prints*, arXiv:2306.10150, doi: [10.48550/arXiv.2306.10150](https://doi.org/10.48550/arXiv.2306.10150)